The Astrophysical Journal, 629:311–327, 2005 August 10

GLOBAL CHARACTERISTICS OF X-RAY FLASHES AND X-RAY–RICH GAMMA-RAY BURSTS OBSERVED BY *HETE-2*

T. Sakamoto,[1,2,3] D. Q. Lamb,[4] N. Kawai,[1,2] A. Yoshida,[2,5] C. Graziani,[4] E. E. Fenimore,[6] T. Q. Donaghy,[4] M. Matsuoka,[7] M. Suzuki,[1] G. Ricker,[8] J.-L. Atteia,[9] Y. Shirasaki,[10] T. Tamagawa,[2] K. Torii,[11] M. Galassi,[6] J. Doty,[8] R. Vanderspek,[8] G. B. Crew,[8] J. Villasenor,[8] N. Butler,[8] G. Prigozhin,[8] J. G. Jernigan,[12] C. Barraud,[9] M. Boer,[13] J.-P. Dezalay,[13] J.-F. Olive,[13] K. Hurley,[12] A. Levine,[8] G. Monnelly,[8] F. Martel,[8] E. Morgan,[8] S. E. Woosley,[14] T. Cline,[3] J. Braga,[15] R. Manchanda,[16] G. Pizzichini,[17] K. Takagishi,[18] and M. Yamauchi[18]

Received 2004 September 7; accepted 2005 April 15

ABSTRACT

We describe and discuss the global properties of 45 gamma-ray bursts (GRBs) observed by *HETE-2* during the first 3 years of its mission, focusing on the properties of X-ray flashes (XRFs) and X-ray–rich GRBs (XRRs). We find that the numbers of XRFs, XRRs, and GRBs are comparable, and that the durations and the sky distributions of XRFs and XRRs are similar to those of GRBs. We also find that the spectral properties of XRFs and XRRs are similar to those of GRBs, except that the values of the peak energy $E_{\rm peak}^{\rm obs}$ of the burst spectrum in νF_ν, the peak energy flux $F_{\rm peak}$, and the energy fluence S_E of XRFs are much smaller (and those of XRRs are smaller) than those of GRBs. Finally, we find that the distributions of all three kinds of bursts form a continuum in the [S_E(2–30 keV), S_E(30–400) keV] plane, the [S_E(2–400 keV), $E_{\rm peak}$] plane, and the [$F_{\rm peak}$(50–300 keV), $E_{\rm peak}$] plane. These results provide strong evidence that all three kinds of bursts arise from the same phenomenon.

Subject heading: gamma rays: bursts

1. INTRODUCTION

Gamma-ray bursts (GRBs) whose energy fluences $S_{\rm X}$ in the X-ray energy band (2–30 keV) are larger than their energy fluences S_γ in the gamma-ray energy band (30–400 keV) have received increasing attention over the last few years. In particular, the Wide Field Camera (WFC) on *BeppoSAX* detected events that were not detected by the Gamma-Ray Burst Monitor (GRBM) on the same satellite. These events have been termed "X-ray flashes" (XRFs; Heise et al. 2001). Throughout this paper, we define "X-ray–rich" GRBs (XRRs) and XRFs as those events for which $\log [S_{\rm X}(2-30\ {\rm keV})/S_\gamma(30-400\ {\rm keV})] > -0.5$ and >0.0, respectively. While arbitrary, these definitions are independent of the properties of any instrument (they can therefore be used by anyone), and the definition of XRFs that we have adopted closely matches the instrument-dependent criterion introduced by Heise et al. (2001) for this kind of burst. Understanding the relationship between XRFs, XRRs, and GRBs may provide a deeper understanding of the prompt emission of GRBs.

2. OBSERVATIONS

In this paper, we investigate the global properties of a sample of the *High Energy Transient Explorer 2* (*HETE-2*) bursts. We require the bursts in this sample to satisfy the following criteria: (1) the burst is detected in the Wide-Field X-Ray Monitor (WXM), (2) the burst is localizable by the WXM, and (3) the signal-to-noise ratio of the WXM data is sufficient to carry out a spectral analysis of the burst. Generally, a joint spectral analysis is carried out for the WXM and the French Gamma Telescope (FREGATE) data. Forty-five bursts observed by *HETE-2* between the beginning of the *HETE-2* mission and 2003 September 13 met these criteria, and this is the sample of bursts that we study.

An important question to consider is the degree to which this sample of bursts may be affected by observational selection effects. A key feature of GRBs (and XRFs and XRRs) is that their spectra are adequately fit by the Band spectral model, which consists of a power-law times exponential cutoff model with a cutoff energy of E_0 and a simple power law that smoothly joins at the so-called "break energy," $E_{\rm break}$ (Band et al. 1993). The value of the low-energy power-law index α is typically in the range of -0.5 to -2, and the value of the high-energy power-law index β

[1] Department of Physics, Tokyo Institute of Technology, 2-12-1 Ookayama, Meguro-ku, Tokyo 152-8551, Japan.
[2] RIKEN (Institute of Physical and Chemical Research), 2-1 Hirosawa, Wako, Saitama 351-0198, Japan.
[3] NASA Goddard Space Flight Center, Greenbelt, MD, 20771.
[4] Department of Astronomy and Astrophysics, University of Chicago, Chicago, IL, 60637.
[5] Department of Physics, Aoyama Gakuin University, Chitosedai 6-16-1, Setagaya-ku, Tokyo 157-8572, Japan.
[6] Los Alamos National Laboratory, P.O. Box 1663, Los Alamos, NM 87545.
[7] Tsukuba Space Center, National Space Development Agency of Japan, Tsukuba, Ibaraki 305-8505, Japan.
[8] Center for Space Research, Massachusetts Institute of Technology, 70 Vassar Street, Cambridge, MA 02139.
[9] Laboratoire d'Astrophysique, Observatoire Midi-Pyreńeés, 14 Avenue Edouard Belin, 31400 Toulouse, France.
[10] National Astronomical Observatory, Osawa 2-21-1, Mitaka, Tokyo 181-8588, Japan.
[11] Department of Earth and Space Science, Graduate School of Science, Osaka University, 1-1 Machikaneyama-cho, Toyonaka, Osaka 560-0043, Japan.
[12] Space Sciences Laboratory, University of California, Berkeley, CA 94720-7450.
[13] Centre d'Etude Spatiale des Rayonnements, CNRS/UPS, B.P. 4346, 31028 Toulouse Cedex 4, France.
[14] Department of Astronomy and Astrophysics, 477 Clark Kerr Hall, University of California, Santa Cruz, CA 95064.
[15] Instituto Nacional de Pesquisas Espaciais, Avenida Dos Astronautas 1758, Saõ Josédos Campos 12227-010, Brazil.
[16] Department of Astronomy and Astrophysics, Tata Institute of Fundamental Research, Homi Bhabha Road, Mumbai 400 005, India.
[17] INAF/IASF Sezione di Bologna, via Gobetti 101, 40129 Bologna, Italy.
[18] Faculty of Engineering, Miyazaki University, Gakuen Kibanadai Nishi, Miyazaki 889-2192, Japan.

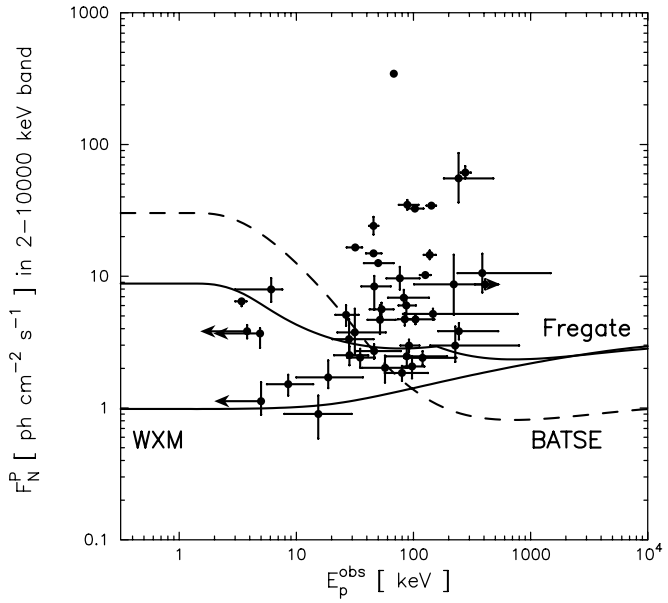

FIG. 1.—Detectability by *HETE-2* of the bursts discussed in this paper. Shown is the $[E^{\rm obs}_{\rm peak},\ F^P_N(2-10{,}000\ {\rm keV})]$ plane, where $E^{\rm obs}_{\rm peak}$ is the observed energy of the peak of the burst spectrum in νF_ν, and $F^P_N(2-10{,}000\ {\rm keV})$ is the peak photon number flux of the burst in the 2–10,000 keV energy band. The solid curves show the WXM and FREGATE thresholds for detecting bursts; the dashed curve shows the BATSE threshold for detecting bursts. The locations of the bursts discussed in this paper are shown as circles along with the 90% confidence region error bars for their values of $E^{\rm obs}_{\rm peak}$ and $F^P_N(2-10{,}000\ {\rm keV})$. After Lamb et al. (2005a).

is typically in the range of -2 to -3.5 for the photon number spectrum of the bursts (which is the spectrum that matters for detecting the burst and for spectral fitting). Hence, the spectra of bursts for which the value of E_0 (and therefore of $E^{\rm obs}_{\rm peak}$) is large have large numbers of photons in the X-ray energy range and are easily detected and localized by an X-ray instrument such as WXM, if they are comparable in brightness and in their time histories to bursts with small values of E_0 (and therefore of $E^{\rm obs}_{\rm peak}$). Consequently, the threshold in peak photon number flux F^P_N for detecting and localizing bursts is relatively independent of the value of E_0 (and therefore of $E^{\rm obs}_{\rm peak}$); i.e., it is relatively independent of whether the burst is an XRF, XRR, or GRB.

Figure 1 illustrates this important point. It shows the thresholds in $F^P_N(2-10{,}000\ {\rm keV})$ for *HETE-2* WXM and FREGATE as a function of $E^{\rm obs}_{\rm peak}$, and the locations of the 45 *HETE-2* bursts discussed in this paper. The figure shows that the threshold for WXM as well as for FREGATE are relatively independent of energy, although the energy band for WXM is 2–25 keV. In particular, the threshold for WXM only increases from $\approx$1 photon cm^{-2} s^{-1} to $\approx$2 photons cm^{-2} s^{-1} in the 2–10,000 keV energy band as $E^{\rm obs}_{\rm peak}$ increases from 1 to 500 keV for a typical burst spectrum with $\alpha = -1$ and $\beta = -2.25$. (The corresponding thresholds in the 2–400 keV energy band are $\approx$2 photons cm^{-2} s^{-1} and $\approx$4 photons cm^{-2} s^{-1}.) The figure also shows that (1) the bursts discussed in this paper form a roughly diagonal distribution that extends down to the threshold of WXM, and (2) the $F^P_N(2-10{,}000\ {\rm keV})$ values of the bursts that are GRBs generally lie well above the threshold of WXM. This is strong evidence that the *HETE-2* WXM is not missing many GRBs relative to XRFs and XRRs because of any observational selection effects related to the differing spectral shapes of the three kinds of bursts.

In this study, we consider three spectral models: (1) a power-law (PL) model whose two parameters are the power-law index α and the normalization constant K_{15} of the spectrum at 15 keV; (2) a power-law times exponential (PLE) model whose three parameters are the power-law index α, the cutoff energy E_0, and K_{15}; and (3) the Band function (Band et al. 1993), whose four parameters are the low-energy power-law index α, the cutoff energy E_0, the high-energy power-law index β, and K_{15}. We determine whether the data require a more complicated model (e.g., the PLE model instead of the PL model, or the Band function instead of the PLE model) using the maximum likelihood ratio test, and whether the data require a significance $Q < 10^{-2}$ in order to adopt the more complicated model.

Table 1 gives some information about the localization and the WXM time histories of the 45 bursts in the sample. Table 2 gives the χ^2 and number of degrees of freedom for all of the spectral fits that we have done. Table 3 gives the details of the fits made to the time-averaged spectral data for each of the bursts, including the class of the burst (e.g., XRF, XRR, GRB) and the spectral parameters of the best-fit spectral model. Table 4 gives the photon number and energy fluence of each burst in the 2–30, 30–400, and 2–400 keV energy bands, and also energy fluence ratios between 2–30 and 30–400 keV. Table 5 gives the photon number peak flux (1 s) of each burst in 2–30, 30–400, 2–400, and 50–300 keV (BATSE [Burst and Transient Source Experiment] channels 3 and 4; Paciesas et al. 1999) bands.

When the WXM photon time- and energy-tagged (TAG) data are available, we apply a "cut" to the WXM data using only the photons from the pixels on wires in the X and Y detectors that were illuminated by the burst and that maximize the S/N, in the same manner as we did for GRB 020531 (D. Q. Lamb et al. 2005a, in preparation). We used the spectral survey data (PHA data for WXM, and SP data for FREGATE) when TAG data were not available. The WXM and FREGATE detector response matrix has been well calibrated using observations of the Crab Nebula (WXM, Shirasaki et al. 2003; FREGATE, Olive et al. 2003). We use the XSPEC version 11.2.0 software package to do the spectral fits. Details of instruments are given in Kawai et al. (2003) and Shirasaki et al. (2003) for the WXM, and in Atteia et al. (2003) for the FREGATE.

The time histories of the bursts, details of the spectral-fitting procedure, and time-resolved spectroscopy of some of the bursts are given in a companion paper (T. Sakamoto et al. 2005, in preparation; see also D. Q. Lamb et al. 2005a, in preparation). Other information about the bursts, including skymaps of the *HETE-2* WXM and soft X-ray camera (SXC) localizations; the FREGATE T_{50} and T_{90} durations of the bursts; whether an X-ray, optical, or radio afterglow was detected; whether a host galaxy has been identified; and the redshift of the burst can be found in the First *HETE-2* Burst Catalog (R. Vanderspek et al. 2005, in preparation).

3. X-RAY AND γ-RAY FLUENCES

The distribution of the fluence ratio $S_{\rm X}(2-30\ {\rm keV})/S_\gamma(30-400\ {\rm keV})$ for the 45 bursts in this study is shown in Figure 2. The boundaries between GRBs and XRRs, and XRRs and XRFs, are shown as dashed lines. The figure clearly shows that XRFs, XRRs, and GRBs form a single broad distribution. The numbers of XRFs, XRRs, and GRBs, are 16, 19, and 10, respectively. The numbers of all three kinds of bursts are roughly equal, modulo the relatively small sample sizes.

Figure 3 shows the distributions of XRFs, XRRs, and GRBs in the $[S_E(2-30\ {\rm keV}),\ S_E(30-400\ {\rm keV})]$ plane. As was evident in Figure 2, the three GRB classes seem to form a single distribution. There is a strong, tight positive correlation between

TABLE 1

SOME PROPERTIES OF 45 *HETE-2* GRBs

GRB	Burst ID	θ_X	θ_Y	TT[a]	TS[b] (s)	EB[c]	R.A.	Decl.	l (deg)	b (deg)	Error [d] (arcmin)	T_{50} (WXM)	T_{90} (WXM)
GRB 010213.....	10805	−2.4	13.6	...	...	...	10 31 36	+05 30 39	239.6	50.3	30.2	8.6 ± 1.2	24.5 ± 1.2
GRB 010225[e].....	1491	−23.1	1.0	G	1.3	5–120	...	...	...	...	...	6.2 ± 1.3	15.9 ± 3.9
GRB 010326B	1496	8.0	−15.0	G	.160	5–120	11 24 24	−11 09 57	271.2	46.3	36	1.7 ± 0.2	5.2 ± 0.2
GRB 010612.....	1546	13.8	1.2	G	.160	30–400	18 03 18	−32 08 01	359.2	−4.9	36	17.4 ± 0.8	28.5 ± 0.2
GRB 010613.....	1547	−30.5	25.2	G	1.3	30–400	17 00 40	+14 16 05	33.9	30.9	36	23.8 ± 1.2	51.8 ± 0.7
GRB 010629B	1573	−26.6	8.3	G	1.3	5–120	16 32 38	−18 43 24	358.6	19.5	15	9.3 ± 0.3	16.2 ± 0.2
GRB 010921.....	1761	−24.0	39.5	G	1.3	5–120	23 01 53	+44 16 12	103.1	−14.3	20 × 15[f]	...	...
GRB 010928.....	1770	−3.0	35.0	G	1.3	30–400	23 28 55	+30 39 11	102.9	−26.7	16.4 × 11[g]	29.5 ± 3.5	59.0 ± 1.8
GRB 011019.....	10823	−18.3	−17.6	...	...	...	00 42 50	−12 26 58	114.7	−75.2	35	12.2 ± 1.3	31.6 ± 1.2
GRB 011103.....	1829	−0.3	−10.9	XG	5.12	...	03 20 37	17 40 01	166.1	−32.4	...	8.6 ± 1.7	19.7 ± 1.2
GRB 011130.....	1864	−13.0	22.8	XG	5.12	...	03 05 36	+03 48 36	174.4	−45.2	10	23.8 ± 0.6	39.5 ± 0.4
GRB 011212.....	10827	−1.6	9.7	...	...	...	05 00 05	+32 07 39	171.8	−6.3	11	33.2 ± 1.2	72.5 ± 2.8
GRB 020124.....	1896	14.7	−31.6	G	1.3	30–400	09 32 49	−11 27 35	244.9	28.3	12	18.6 ± 1.1	50.2 ± 2.3
GRB 020127.....	1902	−7.5	20.8	G	5.12	30–400	08 15 06	+36 44 31	184.7	31.8	8	6.0 ± 0.3	17.6 ± 1.9
GRB 020317.....	1959	−17.1	15.2	G	1.3	5–120	10 23 21	+12 44 38	228.1	52.5	18	2.4 ± 0.4	14.7 ± 0.5
GRB 020331.....	1963	6.9	−14.3	G	.160	30–400	13 16 34	−17 52 29	311.3	44.6	10	35.7 ± 1.8	78.7 ± 1.8
GRB 020531.....	2042	22.9	11.3	G	.020	30–400	15 14 45	−19 21 35	343.6	32.0	38	1.1 ± 0.2	2.5 ± 0.3
GRB 020625.....	2081	5.6	10.1	G	5.2	30–400	20 44 14	+07 10 12	53.3	−21.1	13.8	13.5 ± 1.2	119.2 ± 2.4
GRB 020801.....	2177	4.7	35.4	G	1.3	30–400	21 02 14	−53 46 13	343.9	−40.7	13.9	262.9 ± 4.2	348.9 ± 4.4
GRB 020812.....	2257	−15.3	−12.1	G	1.3	30–400	20 38 48	−05 23 34	40.7	−26.3	13.8	14.1 ± 0.6	42.0 ± 1.0
GRB 020813.....	2262	0.0	−3.8	G	1.3	30–400	19 46 38	−19 35 16	20.8	−20.7	1(S)	>30.0	>89.0
GRB 020819.....	2275	17.7	−22.5	G	.160	30–400	23 27 07	+06 21 50	88.5	−50.8	7	11.5 ± 0.3	46.9 ± 2.0
GRB 020903.....	2314	4.2	12.6	XG	5.12	...	22 49 25	−20 53 59	38.9	−61.5	16.7	4.8 ± 0.4	10.0 ± 0.7
GRB 021004.....	2380	3.9	−12.4	G	5.2	30–400	00 26 57	+18 55 44	114.9	−43.6	2(S)	26.6 ± 1.0	77.1 ± 2.6
GRB 021021.....	10623	15.2	11.9	...	...	...	00 17 23	−01 37 00	103.8	−63.2	20	22.1 ± 1.2	56.5 ± 1.2
GRB 021104.....	2434	22.6	22.9	G	1.3	5–120	03 53 48	+37 57 12	158.1	−12.2	26	10.2 ± 0.5	18.1 ± 0.2
GRB 021112.....	2448	12.2	27.1	G	1.3	5–120	02 36 52	+48 50 56	140.2	−10.5	20	6.8 ± 1.2	14.7 ± 1.1
GRB 021211.....	2493	−12.6	0.0	G	.160	30–400	08 09 00	+06 44 20	215.7	20.3	2(S)	3.1 ± 0.1	13.3 ± 0.3
GRB 030115.....	2533	13.0	−3.1	G	1.3	30–400	11 18 30	+15 02 17	237.4	65.2	2(S)	9.2 ± 0.5	49.6 ± 4.3
GRB 030226.....	10893	−13.0	−16.3	...	...	...	11 33 01	+25 53 56	212.5	72.4	2(S)	66.4 ± 3.9	137.7 ± 4.9
GRB 030323.....	2640	4.1	35.1	XG	.320	...	11 06 54	−21 51 00	273.0	34.9	18	13.9 ± 1.6	32.6 ± 2.7
GRB 030324.....	2641	−26.4	0.6	G	1.3	30–400	13 37 11	−00 19 22	326.6	60.4	7	8.9 ± 0.3	25.8 ± 0.8
GRB 030328.....	2650	5.1	7.1	G	1.3	5–120	12 10 51	−09 21 05	286.4	52.2	1(S)	106.9 ± 1.2	315.8 ± 3.0
GRB 030329.....	2652	26.7	−29.0	G	1.3	5–120	10 44 49	+21 28 44	217.1	60.7	2(S)	12.1 ± 0.2	33.1 ± 0.5
GRB 030416.....	10897	−2.0	−11.3	...	...	...	11 06 51	−02 52 58	258.8	50.8	7	19.7 ± 1.7	61.5 ± 1.2
GRB 030418.....	2686	7.5	−9.7	XG	13.280	...	10 54 53	−06 59 22	259.1	45.7	9	38.7 ± 0.9	117.6 ± 0.7
GRB 030429.....	2695	8.9	11.8	XG	6.72	...	12 13 06	−20 56 00	291.0	41.1	1(S)	38.4 ± 1.5	77.4 ± 1.2
GRB 030519.....	2716	−41.0	16.2	G	.160	30–400	14 58 18	−32 56 57	331.5	22.8	30	6.1 ± 0.6	13.8 ± 0.7
GRB 030528.....	2724	20.7	6.1	G	1.3	30–400	17 04 02	−22 38 59	0.0	11.3	2(S)	20.8 ± 1.2	49.2 ± 1.2
GRB 030723.....	2777	1.6	10.9	XG	6.72	WXM	21 49 30	−27 42 06	21.2	−49.9	2(S)	9.9 ± 0.3	20.2 ± 0.5
GRB 030725.....	2779	18.4	33.1	G	.160	5–120	20 33 47	−50 45 49	348.2	−36.6	14.4	68.3 ± 3.4	200.0 ± 2.5
GRB 030821.....	2814	12.1	32.5	G	1.3	30–400	21 42 33	−45 12 12	354.3	−48.5	120 × 10	11.7 ± 1.5	22.9 ± 0.5
GRB 030823.....	2818	11.7	−32.7	G	5.2	5–120	21 30 47	+21 59 46	73.2	−21.0	5.4	30.2 ± 1.4	66.4 ± 1.9
GRB 030824.....	2821	−29.8	−31.4	G	1.3	5–120	00 05 02	+19 55 37	108.3	−41.6	11.2	13.1 ± 1.8	36.4 ± 0.4
GRB 030913.....	2849	−2.1	4.6	G	1.3	30–400	20 58 02	−02 12 32	46.5	−29.0	30	2.9 ± 0.3	6.7 ± 0.3

NOTE.—Units of right ascension are hours, minutes, and seconds, and units of declination are degrees, arcminutes, and arcseconds.

[a] Triggered type; G: FREGATE triggered, XG: FREGATE triggered by XDSP.

[b] Trigger timescale.

[c] Trigger energy band in keV.

[d] Location error radius (90% confidence). "S" indicates localization by the SXC.

[e] Since the attitude control camera was not operational, the celestial coordinates are not available.

[f] Error is $20^\circ \times 15'$.

[g] Error is $16.'4 \times 11^\circ$.

TABLE 2

THE χ^2 AND dof FOR ALL OF THE SPECTRAL FITS THAT WE HAVE DONE

GRB	χ^2/dof			
	PL[a]	PLE[b]	Band[c]	Comment
GRB 010213	70.2/45	51.3/45	41.4/44*	Fix α for PLE and Band
GRB 010225	43.9/40	36.1/39*	36.1/38	
GRB 010326B	120.2/112	95.0/111*	95.0/110	
GRB 010612	66.6/66	57.5/65*	56.8/64	
GRB 010613	198.8/136	123.2/135	105.2/134*	
GRB 010629B	213.6/111	89.9/110*	90.0/109	
GRB 010921	173.9/141	131.5/140*	131.1/139	
GRB 010928	159.9/126	103.1/125*	102.7/124	
GRB 011019	61.8/68	58.1/68*	58.1/67	Fix α for PLE and Band
GRB 011103	48.1/38*	45.0/37	44.0/36	
GRB 011130	40.7/40*	38.7/39	40.7/38	
GRB 011212	42.9/54*	42.9/53	42.8/52	
GRB 020124	134.6/96	67.5/95*	67.4/94	
GRB 020127	106.4/111	82.1/110*	82.5/109	
GRB 020317	65.7/54	48.9/53*	48.9/52	
GRB 020331	140.2/112	81.3/111*	81.2/110	
GRB 020531	144.7/142	117.2 /141*	117.0/140	
GRB 020625	46.5/55	43.0/55*	43.0/54	Fix α for PLE and Band
GRB 020801	157.3/142	103.0/141	89.3/140*	
GRB 020812	53.3/69	45.2/68*	45.2/67	
GRB 020813	1007.8/142	273.8/141	162.4/140*	
GRB 020819	209.9/110	109.0/109	102.1/108*	
GRB 020903	22.0/26*	22.0/25	21.8/24	
GRB 021004	79.4/69	64.5/68*	63.9/67	
GRB 021021	39.9/41	36.0/41*	43.1/40	Fix α for PLE and Band
GRB 021104	36.1/39	28.3/38*	28.3/37	
GRB 021112	83.6/62	68.7/61*	68.7/60	
GRB 021211	583.7/142	172.3/141	160.9/140*	
GRB 030115	68.8/68	54.4/67*	54.4/66	
GRB 030226	172.1/140	124.2/139*	124.2/138	
GRB 030323	27.6/33*	27.6/32	27.6/31	
GRB 030324	71.2/77	67.1/76*	67.1/75	
GRB 030328	444.4/142	142.0/141	137.5/140*	
GRB 030329	5358.4/141	342.2/140	213.7/139*	
GRB 030416	47.0/54*	53.4/53	47.0/52	
GRB 030418	76.2/69	63.2/68*	63.1/67	
GRB 030429	76.4/69	48.9/68*	48.9/67	
GRB 030519	785.5/126	151.2/125	92.0/124*	
GRB 030528	216.0/111	91.8/110	88.2/109*	
GRB 030723	135.2/142*	136.5/142	136.4/141	Fix α for PLE and Band
GRB 030725	242.1/142	150.7/141*	151.1/140	
GRB 030821	177.1/99	95.1/98*	95.0/97	
GRB 030823	113.1/111	77.9/110*	77.3/109	
GRB 030824	43.1/53*	42.3/52	42.1/51	
GRB 030913	49.4/54	39.2/53*	38.6/52	

NOTE.—The value pairs denoted with an asterisk are for the spectral model that we have chosen as characterizing the spectrum of the burst.

[a] PL: power-law.

[b] PLE: power-law times exponential cutoff.

[c] Band: Band function.

TABLE 3

SPECTRAL PARAMETERS OF 45 *HETE-2* GRBS

GRB	Class[a]	Model[b]	α	β	$E_{\rm peak}$ (keV)	K_{15}[c] (10^{-2} photons cm^{-2} s^{-1} keV^{-1})	χ^2	dof
GRB 010213	XRF	Band	-1.0 (fixed)	$-3.0^{+0.2}_{-0.5}$	3.4 ± 0.4	45^{+8}_{-5}	41.4	44
GRB 010225	XRF	PLE	-1.3 ± 0.3	...	32^{+27}_{-9}	7^{+3}_{-2}	36.1	39
GRB 010326B†	XRR	PLE	$-1.1^{+0.3}_{-0.2}$	...	52^{+19}_{-11}	13^{+3}_{-2}	95.0	111
GRB 010612	GRB	PLE	-1.1 ± 0.2	...	240^{+290}_{-82}	2.9 ± 0.4	57.5	65
GRB 010613	XRR	Band	-1.0 ± 0.3	$-2.0^{+0.1}_{-0.2}$	46^{+18}_{-10}	15^{+4}_{-2}	105.2	134
GRB 010629B	XRR	PLE	-1.1 ± 0.1	...	46^{+5}_{-4}	20 ± 2	89.9	110
GRB 010921†	XRR	PLE	-1.6 ± 0.1	...	89^{+22}_{-14}	42 ± 2	131.5	140
GRB 010928†	GRB	PLE	-0.7 ± 0.1	...	410^{+120}_{-75}	6.3 ± 0.6	103.1	125
GRB 011019	XRF	PLE	-1.4 (fixed)	...	19^{+18}_{-9}	$2.5^{+0.8}_{-0.6}$	58.1	68
GRB 011103†	XRR	PL	$-1.7^{+0.2}_{-0.3}$	...	...	2.7 ± 0.9	48.1	38
GRB 011130	XRF	PL	...	-2.7 ± 0.3	<3.9[d]	0.7 ± 0.3	40.7	40
GRB 011212	XRF	PL	...	-2.1 ± 0.2	...	0.7 ± 0.2	42.9	54
GRB 020124	XRR	PLE	$-0.8^{+0.2}_{-0.1}$	...	87^{+18}_{-13}	9 ± 1	67.5	95
GRB 020127	XRR	PLE	-1.0 ± 0.1	...	100^{+47}_{-24}	$4.5^{+0.6}_{-0.5}$	82.1	110
GRB 020317	XRF	PLE	$-0.6^{+0.6}_{-0.5}$	...	28^{+13}_{-7}	7^{+8}_{-3}	48.9	53
GRB 020331	GRB	PLE	-0.8 ± 0.1	...	92^{+21}_{-14}	$4.0^{+0.5}_{-0.4}$	81.3	111
GRB 020531	GRB	PLE	-0.8 ± 0.1	...	230^{+110}_{-58}	21 ± 2	117.2	141
GRB 020625	XRF	PLE	-1.1 (fixed)	...	$8.5^{+5.4}_{-2.9}$	$2.8^{+1.1}_{-0.8}$	43.0	55
GRB 020801†	GRB	Band	$-0.3^{+0.4}_{-0.3}$	$-2.0^{+0.2}_{-0.3}$	53^{+14}_{-11}	6^{+2}_{-1}	89.3	140
GRB 020812	XRR	PLE	-1.1 ± 0.3	...	88^{+110}_{-30}	$2.3^{+0.6}_{-0.5}$	45.2	68
GRB 020813†	GRB	Band	$-0.94^{+0.03}_{-0.03}$	$-1.57^{+0.03}_{-0.04}$	140^{+14}_{-13}	20.7 ± 0.5	162.4	140
GRB 020819	XRR	Band	$-0.9^{+0.2}_{-0.1}$	$-2.0^{+0.2}_{-0.5}$	50^{+18}_{-12}	11^{+3}_{-2}	102.1	108
GRB 020903	XRF	PL	...	$-2.6^{+0.4}_{-0.6}$	$<5.0(2.6^{+1.4}_{-0.8})$[d]	0.4 ± 0.3	22.0	26
GRB 021004	XRR	PLE	-1.0 ± 0.2	...	80^{+53}_{-23}	$2.8^{+0.6}_{-0.5}$	64.5	68
GRB 021021	XRF	PLE	-1.3 (fixed)	...	15^{+14}_{-8}	$1.2^{+0.5}_{-0.4}$	36.0	41
GRB 021104†	XRF	PLE	-1.1 ± 0.5	...	28^{+17}_{-8}	8^{+5}_{-3}	28.3	38
GRB 021112	XRR	PLE	$-0.9^{+0.4}_{-0.3}$	...	57^{+39}_{-21}	7^{+4}_{-2}	68.7	61
GRB 021211	XRR	Band	-0.9 ± 0.1	$-2.2^{+0.1}_{-0.3}$	46^{+8}_{-6}	33^{+4}_{-3}	160.9	140
GRB 030115	XRR	PLE	-1.3 ± 0.1	...	83^{+53}_{-22}	3.5 ± 0.5	54.4	67
GRB 030226	GRB	PLE	-0.9 ± 0.2	...	97^{+27}_{-17}	3.5 ± 0.4	124.2	139
GRB 030323	XRR	PL	$-1.6^{+0.2}_{-0.3}$	...	...	$2.2^{+0.6}_{-0.7}$	27.6	33
GRB 030324	XRR	PLE	-1.5 ± 0.1	...	150^{+630}_{-65}	$4.9^{+0.7}_{-0.6}$	67.1	76
GRB 030328	GRB	Band	$-1.14^{+0.03}_{-0.03}$	$-2.1^{+0.2}_{-0.4}$	130^{+14}_{-13}	6.6 ± 0.2	137.5	140
GRB 030329	XRR	Band	$-1.26^{+0.01}_{-0.02}$	$-2.28^{+0.05}_{-0.06}$	68 ± 2	146 ± 2	213.7	139
GRB 030416	XRF	PL	...	$-2.3^{+0.1}_{-0.2}$	$<3.8(2.6^{+0.5}_{-1.8})$[d]	0.9 ± 0.2	47.0	54
GRB 030418	XRR	PLE	-1.5 ± 0.1	...	46^{+32}_{-14}	$2.4^{+0.5}_{-0.4}$	63.2	68
GRB 030429	XRF	PLE	$-1.1^{+0.3}_{-0.2}$	...	35^{+12}_{-8}	$4.1^{+1.3}_{-0.9}$	49.0	68
GRB 030519†	GRB	Band	-0.8 ± 0.1	-1.7 ± 0.1	138^{+18}_{-15}	73 ± 2	92.0	124
GRB 030528†	XRF	Band	$-1.3^{+0.2}_{-0.1}$	$-2.7^{+0.3}_{-1.0}$	32 ± 5	14 ± 2	88.2	109
GRB 030723	XRF	PL	...	-1.9 ± 0.2	<8.9[d]	1.0 ± 0.2	135.2	142
GRB 030725	XRR	PLE	$-1.51^{+0.04}_{-0.04}$	...	102^{+19}_{-14}	15.7 ± 0.5	150.7	141
GRB 030821	XRR	PLE	-0.9 ± 0.1	...	84^{+15}_{-11}	$8.7^{+0.8}_{-0.7}$	95.1	98
GRB 030823	XRF	PLE	-1.3 ± 0.2	...	27^{+8}_{-5}	8 ± 2	77.9	110
GRB 030824	XRF	PL	...	-2.1 ± 0.1	$<8.7(6.1^{+1.9}_{-4.2})$[d]	5.3 ± 0.8	43.1	53
GRB 030913	GRB	PLE	$-0.8^{+0.3}_{-0.2}$	...	120^{+110}_{-37}	$3.5^{+0.8}_{-0.7}$	39.2	53

NOTE.—Daggers denote that the constant factor is multiplied by the spectral model.

[a] GRB classification—XRF: X-ray-flash; XRR: X-ray–rich GRB; GRB: GRB.

[b] Spectral model—PL: power-law; PLE: power-law times exponential cutoff; Band: Band function.

[c] Normalization at 15 keV.

[d] 99.7% upper limit and 90% confidence interval (in parentheses) derived by the *constrained* Band function.

TABLE 4

PHOTON NUMBER AND PHOTON ENERGY FLUENCES OF 45 *HETE-2* GRBs

GRB	DURATION (s)	PHOTON FLUENCE (photons cm^{-2})			ENERGY FLUENCE (10^{-7} ergs cm^{-2})			X-RAY/γ-RAY RATIO
		2–30 keV	30–400 keV	2–400 keV	2–30 keV	30–400 keV	2–400 keV	
GRB 010213	34.4	111 ± 5	$0.7^{+0.7}_{-0.3}$	112 ± 5	$7.9^{+0.3}_{-0.5}$	$0.7^{+0.6}_{-0.3}$	9 ± 1	11.4
GRB 010225	9.8	28 ± 4	$2.7^{+1.0}_{-0.9}$	31 ± 4	3.5 ± 0.4	$2.4^{+1.7}_{-0.9}$	6^{+2}_{-1}	1.5
GRB 010326B	3.5	17 ± 3	$3.2^{+0.5}_{-0.6}$	20 ± 3	$2.4^{+0.3}_{-0.3}$	3 ± 1	6 ± 1	0.8
GRB 010612	47.2	57^{+13}_{-12}	29 ± 2	86^{+14}_{-12}	$8.8^{+1.4}_{-1.3}$	50^{+7}_{-6}	59 ± 7	0.2
GRB 010613	141.6	672^{+110}_{-91}	169 ± 6	840^{+110}_{-92}	102 ± 7	228 ± 13	329 ± 14	0.5
GRB 010629B	24.6	183 ± 20	30 ± 2	213 ± 20	$25.4^{+1.7}_{-1.7}$	$28.6^{+2.7}_{-2.5}$	$54.0^{+3.3}_{-3.1}$	0.9
GRB 010921	23.9	610^{+49}_{-46}	89 ± 4	699^{+48}_{-46}	72 ± 3	113^{+9}_{-8}	184 ± 10	0.6
GRB 010928	34.6	71^{+10}_{-9}	105^{+3}_{-3}	175^{+10}_{-9}	$13.7^{+1.2}_{-1.4}$	226^{+9}_{-10}	239^{+9}_{-5}	0.1
GRB 011019	24.6	28 ± 6	$1.5^{+1.2}_{-1.0}$	29 ± 6	3.0 ± 0.6	$1.1^{+1.4}_{-0.7}$	$4.1^{+1.5}_{-1.1}$	2.8
GRB 011103	14.8	31 ± 5	4^{+4}_{-2}	35^{+7}_{-6}	$3.3^{+0.8}_{-0.7}$	6^{+9}_{-3}	10^{+9}_{-4}	0.5
GRB 011130	50.0	86 ± 13	$1.0^{+1.0}_{-0.5}$	87 ± 13	$5.9^{+1.0}_{-1.0}$	$1.0^{+1.2}_{-0.6}$	$6.8^{+1.9}_{-1.5}$	6.0
GRB 011212	57.7	47 ± 7	$2.3^{+1.7}_{-0.6}$	50^{+8}_{-7}	$4.2^{+0.6}_{-0.6}$	$3.4^{+2.5}_{-1.7}$	$7.6^{+2.9}_{-2.2}$	1.3
GRB 020124	40.6	115 ± 12	51 ± 4	166^{+13}_{-12}	19.7 ± 1.4	61^{+9}_{-8}	81^{+9}_{-8}	0.3
GRB 020127	25.6	44 ± 4.1	$15.6^{+1.8}_{-1.5}$	59 ± 5	6.7 ± 0.5	21^{+5}_{-4}	27 ± 4	0.3
GRB 020317	10.0	14^{+4}_{-3}	$1.7^{+0.8}_{-0.7}$	16^{+4}_{-3}	$2.2^{+0.4}_{-0.4}$	$1.3^{+0.9}_{-0.6}$	$3.5^{+0.9}_{-0.8}$	1.7
GRB 020331	75.0	93^{+8}_{-7}	44 ± 4	137 ± 8	16 ± 1.0	53^{+9}_{-7}	69^{+9}_{-8}	0.3
GRB 020531	1.0	7.5 ± 1.1	6.2 ± 0.5	13.7 ± 1.2	1.3 ± 0.1	$11.1^{+1.4}_{-1.3}$	12.3 ± 1.4	0.1
GRB 020625	41.9	25 ± 4	$0.2^{+0.5}_{-0.2}$	25 ± 4	$2.4^{+0.6}_{-0.5}$	$0.1^{+0.4}_{-0.1}$	$2.5^{+0.8}_{-0.6}$	20.5
GRB 020801	118.0	131^{+27}_{-24}	70 ± 5	201^{+27}_{-24}	26 ± 3	95 ± 11	121 ± 11	0.3
GRB 020812	60.2	53 ± 10	16^{+4}_{-3}	69^{+11}_{-10}	8 ± 1	19^{+8}_{-6}	27^{+8}_{-6}	0.4
GRB 020813	113.0	845^{+23}_{-21}	480 ± 5	1325^{+24}_{-22}	139^{+3}_{-2}	840^{+12}_{-13}	979 ± 13	0.2
GRB 020819	50.2	163 ± 9	46^{+4}_{-3}	209 ± 10	$25.2^{+1.1}_{-1.1}$	63^{+8}_{-9}	88^{+8}_{-10}	0.4
GRB 020903	13.0	13 ± 3	$0.2^{+0.3}_{-0.1}$	13 ± 3	$0.8^{+0.3}_{-0.2}$	$0.2^{+0.4}_{-0.1}$	$1.0^{+0.6}_{-0.3}$	7.3
GRB 021004	49.7	50 ± 5	15 ± 3	65 ± 6	7.7 ± 0.7	18^{+7}_{-5}	26^{+7}_{-5}	0.4
GRB 021021	49.2	23^{+5}_{-5}	$0.9^{+1.1}_{-0.7}$	24^{+5}_{-6}	2.5 ± 0.6	$0.6^{+1.1}_{-0.5}$	$3.1^{+1.4}_{-1.1}$	4.0
GRB 021104	31.4	79^{+30}_{-21}	$7.5^{+3.1}_{-2.5}$	86^{+30}_{-21}	10 ± 2	6^{+4}_{-3}	16^{+5}_{-3}	1.7
GRB 021112	4.0	9 ± 2	2.1 ± 0.6	11 ± 2	1.3 ± 0.3	$2.1^{+1.1}_{-0.9}$	$3.5^{+1.1}_{-0.9}$	0.6
GRB 021211	8.0	74.6 ± 2.4	18.9 ± 0.9	93.4 ± 2.6	11.6 ± 0.3	23.7 ± 2.0	35.3 ± 2.1	0.5
GRB 030115	36.0	59 ± 5	$12.6^{+1.4}_{-1.8}$	71 ± 6	7.9 ± 0.6	15^{+4}_{-3}	23^{+4}_{-3}	0.5
GRB 030226	68.8	80 ± 10	33 ± 3	114^{+10}_{-11}	13 ± 1	43^{+7}_{-6}	56^{+7}_{-6}	0.3
GRB 030323	19.6	29^{+16}_{-13}	$5.5^{+1.6}_{-1.8}$	35^{+16}_{-13}	$3.4^{+1.3}_{-1.2}$	9 ± 4	12^{+4}_{-3}	0.4
GRB 030324	15.7	44^{+5}_{-4}	9.0 ± 1.3	53 ± 5	5.5 ± 0.4	13 ± 3	18 ± 3	0.4
GRB 030328	199.2	556^{+12}_{-10}	193^{+6}_{-4}	751 ± 12	82 ± 1	287 ± 14	370 ± 14	0.3
GRB 030329	62.9	4120^{+41}_{-42}	843 ± 6	4960 ± 40	553 ± 3	1076^{+13}_{-14}	1630^{+14}_{-13}	0.5
GRB 030416	78.6	114 ± 10	$3.2^{+1.6}_{-0.8}$	117 ± 10	9.0 ± 0.9	$3.7^{+1.9}_{-1.4}$	13^{+3}_{-2}	2.4
GRB 030418	110.1	143 ± 9	17^{+4}_{-3}	161^{+9}_{-10}	17.1 ± 1.1	17^{+7}_{-5}	35^{+7}_{-6}	1.0
GRB 030429	24.6	35^{+5}_{-4}	$4.4^{+1.0}_{-1.2}$	40 ± 5	4.7 ± 0.5	$3.8^{+1.4}_{-1.2}$	$8.5^{+1.5}_{-1.3}$	1.3
GRB 030519	21.0	486^{+25}_{-24}	358^{+2}_{-4}	843 ± 24	$87.1^{+2.4}_{-2.4}$	610 ± 10	697 ± 10	0.1
GRB 030528	83.6	512^{+40}_{-39}	54 ± 3	566^{+40}_{-38}	62 ± 3	56 ± 7	119 ± 8	1.1
GRB 030723	31.3	29 ± 4	$0.6^{+3.3}_{-0.5}$	29^{+8}_{-5}	2.8 ± 0.5	$0.4^{+5.6}_{-0.3}$	$3.2^{+5.8}_{-0.8}$	7.5
GRB 030725	83.9	785 ± 28	127 ± 4	912^{+29}_{-28}	94 ± 2	167 ± 10	261^{+11}_{-10}	0.6
GRB 030821	21.2	61 ± 6	$23.1^{+1.5}_{-1.5}$	84 ± 6	10.0 ± 0.6	28 ± 3	37 ± 3	0.4
GRB 030823	55.6	191^{+18}_{-17}	16 ± 3	207 ± 18	$23.1^{+1.6}_{-1.6}$	13 ± 4	36^{+5}_{-4}	1.8
GRB 030824	15.7	103 ± 15	4.7 ± 1.4	108 ± 15	8.9 ± 1.1	$5.8^{+2.4}_{-1.9}$	15^{+3}_{-2}	1.5
GRB 030913	9.1	10.5 ± 1.8	5.8 ± 0.8	16 ± 2	1.8 ± 0.2	8^{+3}_{-2}	10^{+3}_{-2}	0.2

TABLE 5

PEAK (1 s) PHOTON NUMBER FLUX OF 45 *HETE-2* GRBs

GRB	Class[a]	Model[b]	$F^N_{\mathrm{peak}(2-30\ \mathrm{keV})}$ (photons cm^{-2} s^{-1})	$F^N_{\mathrm{peak}(30-400\ \mathrm{keV})}$	$F^N_{\mathrm{peak}(2-400\ \mathrm{keV})}$	$F^N_{\mathrm{peak}(50-300\ \mathrm{keV})}$
GRB 010213	XRF	Band	6.3 ± 0.8	$(3.0 \pm 0.6) \times 10^{-3}$	6.3 ± 0.8	$(1.1 \pm 0.2) \times 10^{-2}$
GRB 010225	XRF	PLE	5.1 ± 2.4	0.3 ± 0.2	5.5 ± 2.4	$(9.6 \pm 9.4) \times 10^{-2}$
GRB 010326B	XRR	PLE	11 ± 3	1.5 ± 0.4	12 ± 3	0.7 ± 0.2
GRB 010612	GRB	PLE	4.3 ± 1.2	4.4 ± 0.5	8.7 ± 1.4	3.1 ± 0.4
GRB 010613	XRR	Band	25 ± 12	2.7 ± 0.9	27 ± 11	1.2 ± 0.4
GRB 010629B	XRR	PLE	39 ± 7	4.2 ± 0.4	43 ± 7	1.9 ± 0.3
GRB 010921	XRR	PLE	34 ± 4	5.7 ± 0.5	40 ± 4	3.2 ± 0.3
GRB 010928	GRB	PLE	3.8 ± 0.8	6.9 ± 0.5	11 ± 1	5.0 ± 0.5
GRB 011019	XRF	PL	3.6 ± 1.4	0.2 ± 0.1	3.8 ± 1.4	$(7.4 \pm 7.3) \times 10^{-2}$
GRB 011103	XRR	PL	4.4 ± 1.1	0.1 ± 0.1	4.6 ± 1.1	$(6.5 \pm 4.3) \times 10^{-2}$
GRB 011130	XRF	PL	5.3 ± 1.3	$(8.2 \pm 6.3) \times 10^{-2}$	5.4 ± 1.3	$(3.6 \pm 3.2) \times 10^{-2}$
GRB 011212	XRF	PL	1.1 ± 1.0	$<7.7 \times 10^{-2}$	1.1 ± 1.0	$<4.4 \times 10^{-2}$
GRB 020124	XRR	PLE	6.9 ± 1.6	2.5 ± 0.4	9.4 ± 1.8	1.4 ± 0.3
GRB 020127	XRR	PLE	6.0 ± 1.2	2.2 ± 0.4	8.1 ± 1.5	1.3 ± 0.3
GRB 020317	XRF	PLE	4.6 ± 1.0	0.6 ± 0.3	5.3 ± 1.1	0.2 ± 0.1
GRB 020331	GRB	PLE	1.9 ± 0.4	1.7 ± 0.2	3.7 ± 0.5	1.2 ± 0.2
GRB 020531	GRB	PLE	17 ± 5	5.6 ± 0.7	23.0 ± 4.7	3.6 ± 0.5
GRB 020625	XRF	PL	2.9 ± 1.0	0.3 ± 0.2	3.2 ± 1.1	0.2 ± 0.1
GRB 020801	GRB	Band	6.4 ± 1.1	1.4 ± 0.3	7.7 ± 2.1	0.8 ± 0.2
GRB 020812	XRR	PLE	2.5 ± 0.8	0.8 ± 0.3	3.3 ± 1.0	0.5 ± 0.2
GRB 020813	GRB	Band	20 ± 1	13 ± 1	32 ± 2	8.3 ± 0.6
GRB 020819	XRR	Band	12 ± 1	5.6 ± 0.4	18 ± 1	3.4 ± 0.3
GRB 020903	XRF	PL	2.8 ± 0.7	$3.2^{+6.7}_{-2.4} \times 10^{-2}$	2.8 ± 0.7	$1.4^{+3.7}_{-1.1} \times 10^{-2}$
GRB 021004	XRR	PLE	1.8 ± 0.4	0.9 ± 0.2	2.7 ± 0.5	0.4 ± 0.2
GRB 021021	XRF	PL	2.1 ± 1.1	0.3 ± 0.2	2.5 ± 1.2	0.2 ± 0.2
GRB 021104	XRF	PLE	4.2 ± 1.8	0.7 ± 0.2	4.9 ± 1.8	0.3 ± 0.1
GRB 021112	XRR	PLE	3.5 ± 1.2	1.0 ± 0.4	4.5 ± 1.3	0.6 ± 0.3
GRB 021211	XRR	Band	22 ± 1	8.4 ± 0.6	30 ± 2	4.1 ± 0.3
GRB 030115	XRR	PLE	7.0 ± 1.3	1.2 ± 0.2	8.1 ± 1.4	1.2 ± 0.2
GRB 030226	GRB	PLE	1.7 ± 0.5	1.0 ± 0.2	2.7 ± 0.6	0.6 ± 0.1
GRB 030323	XRR	PL	3.4 ± 2.1	0.5 ± 0.2	3.9 ± 2.1	0.3 ± 0.2
GRB 030324	XRR	PLE	6.6 ± 1.0	1.6 ± 0.3	8.3 ± 1.2	1.0 ± 0.2
GRB 030328	GRB	Band	6.7 ± 0.5	4.9 ± 0.3	11.6 ± 0.9	3.3 ± 0.2
GRB 030329	XRR	Band	379 ± 21	72 ± 4	451 ± 25	38 ± 2
GRB 030416	XRF	PL	4.5 ± 0.9	0.3 ± 0.1	4.8 ± 0.9	$(1.4 \pm 0.6) \times 10^{-2}$
GRB 030418	XRR	PLE	3.7 ± 0.9	0.3 ± 0.2	4.0 ± 0.9	0.1 ± 0.1
GRB 030429	XRF	PLE	3.1 ± 0.7	0.7 ± 0.2	3.8 ± 0.8	0.3 ± 0.1
GRB 030519	GRB	Band	7.5 ± 3.4	12 ± 5	19 ± 8	8 ± 3
GRB 030528	XRF	Band	17.3 ± 1.5	0.6 ± 0.1	17.9 ± 1.6	$(1.5 \pm 0.6) \times 10^{-1}$
GRB 030723	XRF	PLE	2.0 ± 0.4	0.1 ± 0.1	2.1 ± 0.4	$3.1^{+9.4}_{-2.6} \times 10^{-2}$
GRB 030725	XRR	PLE	25 ± 2	9.1 ± 0.6	34 ± 2	5.7 ± 0.4
GRB 030821	XRR	PLE	3.8 ± 0.7	1.9 ± 0.3	5.8 ± 0.9	1.2 ± 0.2
GRB 030823	XRF	PLE	7.0 ± 1.6	0.6 ± 0.3	7.6 ± 1.7	0.2 ± 0.1
GRB 030824	XRF	PL	12 ± 4	0.3 ± 0.1	12.7 ± 3.8	$(1.3 \pm 0.7) \times 10^{-1}$
GRB 030913	GRB	PLE	2.2 ± 0.5	1.4 ± 0.3	3.6 ± 0.6	0.9 ± 0.2

[a] GRB classification—XRF: X-ray-flash; XRR: X-ray–rich GRB; GRB: GRB.

[b] Spectral model—PL: power-law; PLE: power-law times exponential cutoff; Band: Band function.

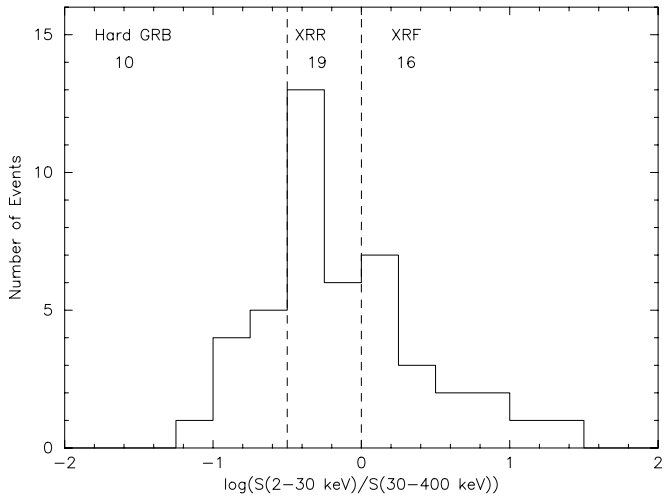

FIG. 2.—Distribution of the fluence ratio $S_E(2-30\ \mathrm{keV})/S_E(30-400\ \mathrm{keV})$. The dashed lines correspond to the borders between hard GRBs and XRRs, and between XRRs and XRFs.

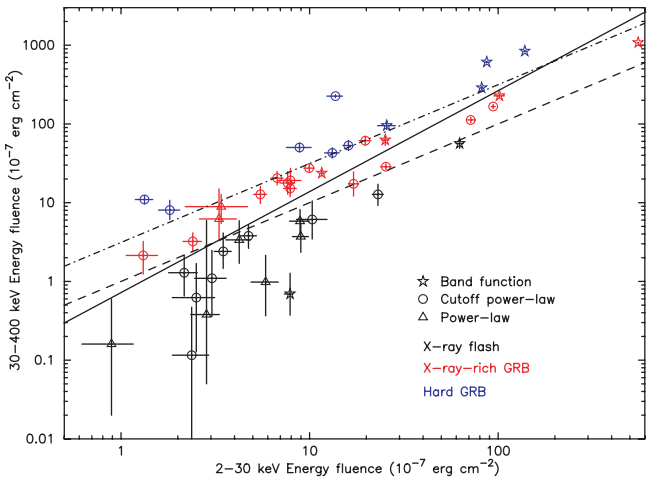

FIG. 3.—Distribution of the bursts in this study in the [$S_E(2–30\ \mathrm{keV})$, $S_E(30–400\ \mathrm{keV})$] plane. The dashed line corresponds to the boundary between XRFs and XRRs. The dot-dashed line corresponds to the boundary between XRRs and GRBs. The solid line is the best linear fit to the burst distribution and is given by $S_E(30-400\ \mathrm{keV}) = (0.722 \pm 0.161) \times S_E(2-30\ \mathrm{keV})^{1.282\pm0.082}$. The correlation coefficient of the burst distribution is 0.851. The probability of such a correlation occurring by chance for the sample size of 45 bursts is 1.1×10^{-8}.

$S_E(2–30\ \mathrm{keV})$ and $S_E(30–400\ \mathrm{keV})$: $S_E(30-400\ \mathrm{keV}) = (0.722 \pm 0.161) \times S_E(2-30\ \mathrm{keV})^{1.282\pm0.082}$. The values of the slope and the uncertainty in the slope that we find imply a significance for the correlation of $\sim$15 σ. The correlation coefficient of +0.851 that we find between the two quantities also implies a high significance for the correlation; the probability of such a correlation occurring by chance for the sample size of 45 bursts is 1.1×10^{-8}. The tightness of the correlation implies that there are no bursts in the *HETE-2* sample with a high X-ray fluence and a low γ-ray fluence, or vice versa.

4. DURATIONS

Figure 4 shows the distributions of T_{50} (Fig. 4*a*) and T_{90} (Fig. 4*b*) durations in the WXM energy band 2–25 keV for each kind of GRB. For comparison, we also show the distributions of T_{50} and T_{90} durations for the BATSE bursts (Paciesas et al. 1999).

The durations of the brightest peaks of GRBs show a strong dependence on the energy band in which they are measured (Fenimore et al. 1995), as does the overall duration of the bursts (Norris et al. 2000), with both $\propto E^{\sim -0.4}$. Therefore, one might expect the T_{50} and T_{90} distributions for XRFs, XRRs, and GRBs to be different, and the T_{50} and T_{90} distributions for XRFs and XRRs to differ from those for long BATSE bursts, particularly since the durations of the latter were measured in a higher energy band. We have used the Kolmogorov-Smirnov (K-S) test to investigate this possibility. Applying this test to the T_{50} distributions for XRFs and GRBs, XRRs and GRBs, and XRF and XRRs, we find K-S test probabilities of 0.25, 0.47, and 0.88, respectively. For the T_{90} distribution, we find K-S test probabilities for the same cross-comparisons of 0.97, 0.99, and 0.91, respectively. Applying the K-S test to the T_{50} distributions for XRFs plus XRRs and long ($T_{50} > 2$ s) BATSE bursts, and for XRFs and long BATSE bursts, we find K-S probabilities of 0.42 and 0.74, respectively. For the T_{90} distribution, we find K-S test probabilities for the same cross-comparisons of 0.66 and 0.55, respectively.

These K-S tests reveal no statistically significant evidence that the distributions of T_{50} and T_{90} durations for XRFs, XRRs, and GRBs are different, or that the distributions of T_{50} and T_{90} durations for XRFs and XRRs plus GRBs are different from those for long BATSE bursts. The last result is consistent with the conclusion reached by Kippen et al. (2003), who found no statistically significant evidence that the T_{50} and T_{90} distributions of *BeppoSAX* WFC XRFs and long *Compton Gamma Ray Observatory* (*CGRO*) BATSE bursts differ. However, we caution that the size of the current *HETE-2* samples of XRFs, XRRs, and GRBs is small, as is the size of the sample of *BeppoSAX* WFC XRFs, and therefore the power of these K-S tests is small.

5. SKY DISTRIBUTIONS

Figure 5 shows the sky distribution in ecliptic coordinates of the 44 *HETE-2* XRFs, XRRs, and GRBs in this study.[19] The *HETE-2* sky coverage is not uniform, and as a result it is difficult to make a meaningful statement about the sky distributions of these three kinds of GRBs. Modulo this and the relatively small sample size of each of the three kinds of bursts, there is no statistically significant evidence that the sky distributions of the three kinds of bursts are different.

6. DISTRIBUTION OF SPECTRAL PARAMETERS

We find that a simple PL model provides an adequate fit to the spectral data for eight of the 45 bursts in this study (six XRFs and two XRRs). In the case of the six bursts we classify as XRFs, the slope of the power-law index is < -2. We interpret this result as follows. The spectral data for these bursts do not constrain $E^{\mathrm{obs}}_{\mathrm{peak}}$, but the fact that $\beta < -2$ means that we are observing the high-energy power-law portion of their Band-model spectra, and $E^{\mathrm{obs}}_{\mathrm{peak}}$ is near or below 2 keV, the lower limit of the WXM energy band. We therefore conclude that these are XRFs.

In the case of the four XRRs, the normalization constants, K_{15}, of the spectra are the lowest among all of the XRRs and GRBs. We therefore interpret the lack of evidence for $E^{\mathrm{obs}}_{\mathrm{peak}}$ in these bursts as due to the low signal-to-noise ratio of their spectra. In these cases, it is difficult to constrain the break energy, E_0, and a power-law model gives an adequate fit to the spectral data.

[19] Since the attitude control camera was not operational, the celestial coordinates of GRB 010225 are not available.

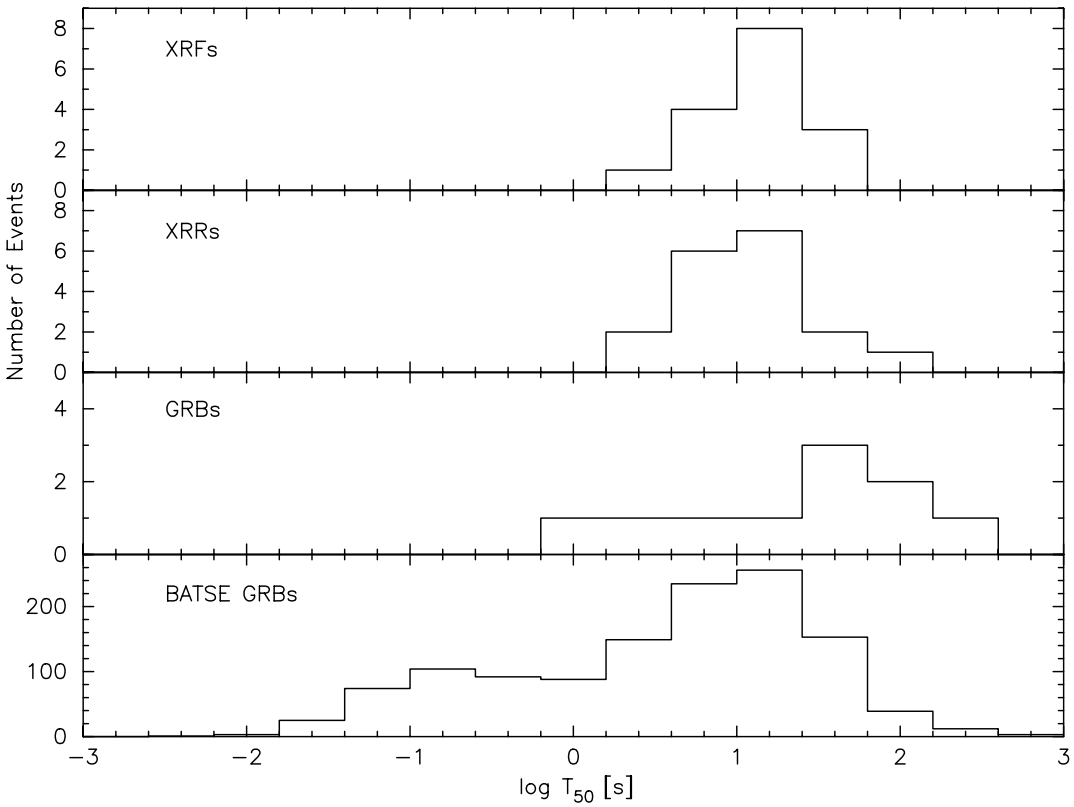

FIG. 4*a*

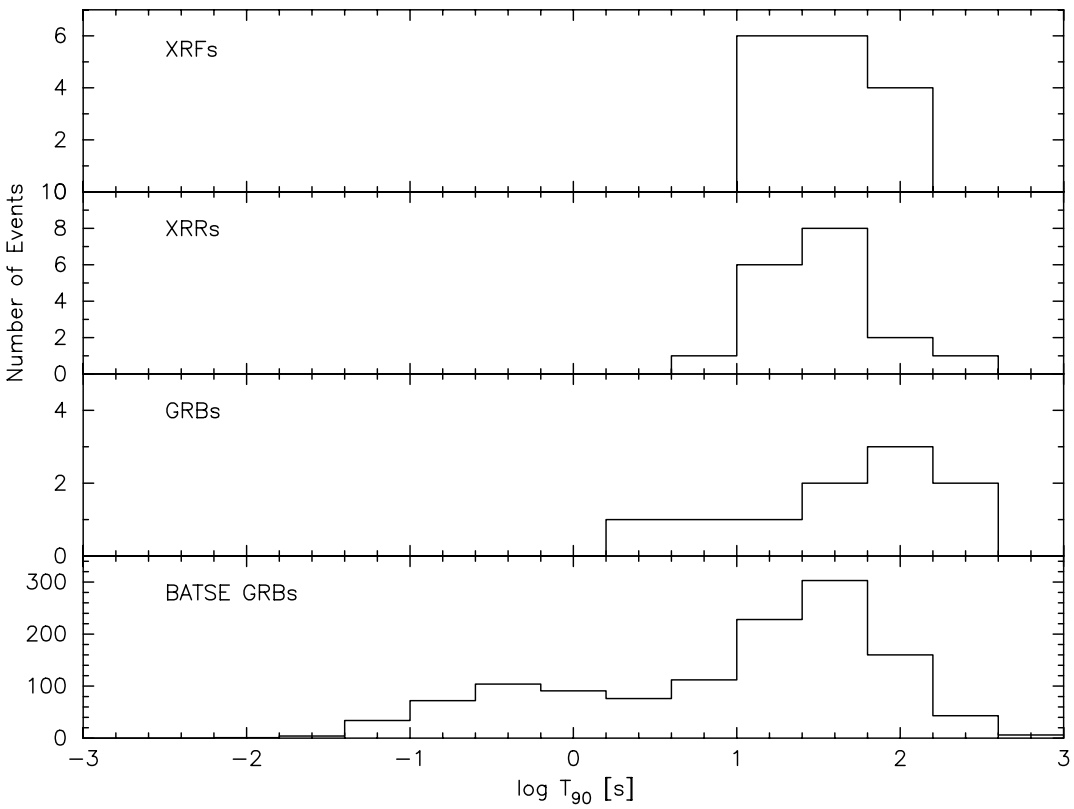

FIG. 4*b*

FIG. 4.—Comparison between (*a*) T_{50} and (*b*) T_{90} measures of burst duration in the 2–25 keV energy band for the three kinds of bursts seen by *HETE-2*, and in the 50–300 keV energy band for BATSE GRBs. The panels in (*a*) and (*b*) show (from top to bottom) the distribution of the durations of XRFs, XRRs, GRBs, and BATSE GRBs. The duration of the BATSE sample includes not only the long GRBs but also the short GRBs. There is no statistically significant evidence for any differences between the T_{50} and T_{90} durations of XRFs, XRRs, and GRBs, or between XRFs and long BATSE bursts (see the text for details).

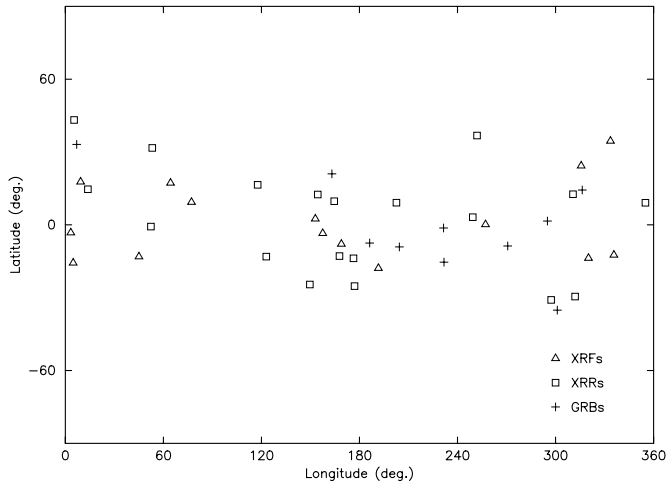

FIG. 5.—Comparison of the sky distributions in ecliptic coordinates for all of the *HETE-2* bursts in this study.

We find that the PLE model is preferred at a significance $Q < 10^{-2}$ over the PL model and provides an adequate fit to the spectral data for 27 of the 45 bursts in this study (eight XRFs, 13 XRRs, and six GRBs). The Band model is preferred at a significance $Q < 10^{-2}$ over the PLE model and provides an adequate fit to the spectral data for the remaining 10 bursts (one XRF, five XRRs, and four GRBs) in this study.

Two of the bursts for which the Band model is preferred by the data over the PLE model and provides an adequate fit to the spectral data have values of the high-energy power-law index $\beta > -2$ (GRBs 020813 and 030519). We do not include these two bursts in the sample of bursts whose spectral properties we now discuss, because the $E^{\rm obs}_{\rm peak}$ found by fitting to the *HETE-2* WXM and FREGATE data lies near or above the upper limit of the FREGATE energy band and is not the actual energy of the peak of the burst spectrum in νF_ν. Therefore the high-energy power law in the Band model that we fit to the *HETE-2* data is not the actual β in the Band-model spectrum.

Table 2 gives both the χ^2 and the number of degrees of freedom (dof) for all of the spectral fits that we have done. In this table, we show with asterisks the models that are preferred at a significance $Q < 10^{-2}$ and that provide an adequate fit to the data. These are the models that we have chosen as characterizing the burst-averaged spectra of the bursts in this study. Tables 3, 4, and 5 give the spectral parameters for the chosen model, the photon number and photon energy fluences in various energy bands, and the photon number and photon energy peak fluxes in various energy bands, for the 45 bursts in this study.

6.1. *Distribution of α-Values*

Figure 6 shows the distribution of the low-energy photon index α. In this figure, we include bursts that require the PLE model or the Band model in order to adequately represent their energy spectra. We do not include bursts whose spectra are adequately represented by a simple PL model, since in this case the photon index of the PL model is most likely the high-energy photon index β of the Band model.

There is a well-known systematic effect when fitting the PLE model to a spectrum whose shape is that of the Band model but for which the energy range or the signal-to-noise ratio of the observations is insufficient to require the Band model; the low-energy power-law index α is smaller (more negative) than it would otherwise be, and the peak energy $E^{\rm obs}_{\rm peak}$ of the spectrum in νF_ν is larger than it would otherwise be (see Fig. 3 of Band et al. 1993). This systematic effect must be kept in mind when comparing bursts for which the PLE model adequately represents the data and bursts for which the Band model is required to adequately represent the data. We therefore show the α-values for burst spectra requiring the Band model as hatched regions, and the α-values for burst spectra that are adequately fit by the PLE model as nonhatched regions. However, there is no clear evidence in Figure 6 of the above systematic effect.

The distribution of the low-energy photon index α clusters around -1, and is similar to the BATSE distribution of α-values (Preece et al. 2000). The relatively small number of bursts with $\alpha > -0.5$ in the *HETE-2* burst sample compared to the BATSE sample of bright bursts (Preece et al. 2000) could have three possible explanations: (1) the *HETE-2* burst sample might be lacking very hard GRBs because such bursts are relatively more difficult for the WXM to detect and to localize; (2) the *HETE-2* values are for time-averaged burst spectra, whereas the α-values reported for the BATSE sample of bright bursts by Preece et al. (2000) are for time-resolved spectra; and (3) the PLE model provides an adequate fit to the spectra for most of the *HETE-2* bursts, and therefore the value of α is systematically more negative than it would otherwise be, as mentioned above. The first scenario is unlikely because, even if very hard GRBs had peak fluxes and fluences that were comparable to those of softer GRBs, *HETE-2* would be unlikely to miss them, as Figure 1 shows—but very hard GRBs have, in fact, larger peak fluxes and fluences than do softer bursts (Mallozzi et al. 1995; Preece et al. 2000). The second scenario may play a role, since it is well known that the spectra of most bursts are hardest at or near the peak of the burst time history and softer afterward. We regard the third scenario as the most likely, since the vast majority of the 5000 time-resolved burst spectra in the BATSE sample were fit using the Band model.

Applying the K-S test to the distributions of α for XRFs and GRBs, XRRs and GRBs, and XRF and XRRs (see Fig. 6*a*), we find K-S test probabilities of 0.27, 0.79, and 0.21, respectively. Thus there is no statistically significant evidence that the distributions of α-values for the burst-averaged spectra of XRFs, XRRs, and GRBs are different. However, this conclusion is a weak one, given the current small sample sizes of *HETE-2* XRFs, XRRs, and GRBs, and the presence of the above systematic effect.

6.2. *Distribution of $E^{\rm obs}_{\rm peak}$ and β-Values*

Figure 7 shows the distribution of the values of the observed peak energy $E^{\rm obs}_{\rm peak}$ of the burst spectra in νF_ν. The events labeled with left-pointing arrows are the 99.7% upper limits for $E^{\rm obs}_{\rm peak}$ derived using the *constrained* Band function. A detailed description of the *constrained* Band function is given in Sakamoto et al. (2004). The distribution of $E^{\rm obs}_{\rm peak}$ values is clearly distorted by the systematic effect mentioned above; i.e., bursts for which the PLE model provides an adequate representation of the data have values of $E^{\rm obs}_{\rm peak}$ that are larger than they would otherwise be. Despite this systematic effect, the distribution of $E^{\rm obs}_{\rm peak}$ values for the sample of *HETE-2* GRBs is much broader than that for the BATSE sample of time-resolved spectra of bright bursts (Preece et al. 2000). In particular, the distribution of $E^{\rm obs}_{\rm peak}$ values in the *HETE-2* burst sample extends to much lower energies. There are clear differences between the $E^{\rm obs}_{\rm peak}$ distributions for XRFs, XRRs, and GRBs, but this is simply because of the strong correlation that must exist between $E^{\rm obs}_{\rm peak}$ and the fluence ratio $S_E(2-30\ {\rm keV})/S_E(30-400\ {\rm keV})$.

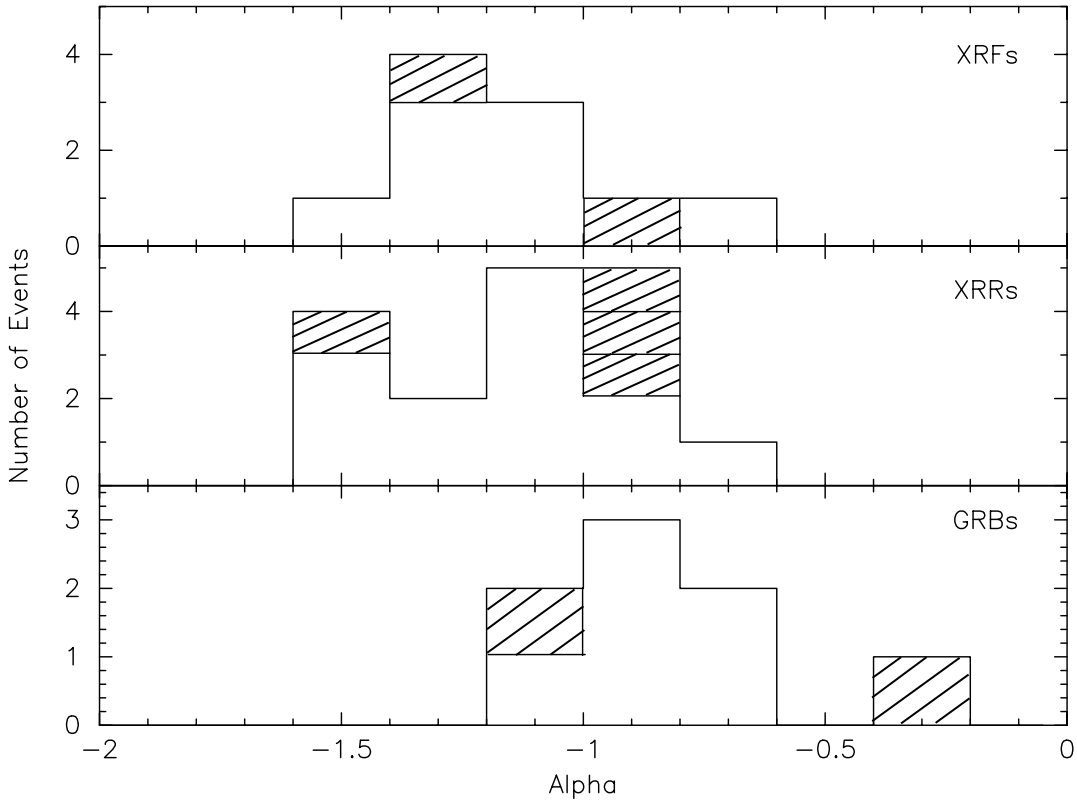

FIG. 6*a*

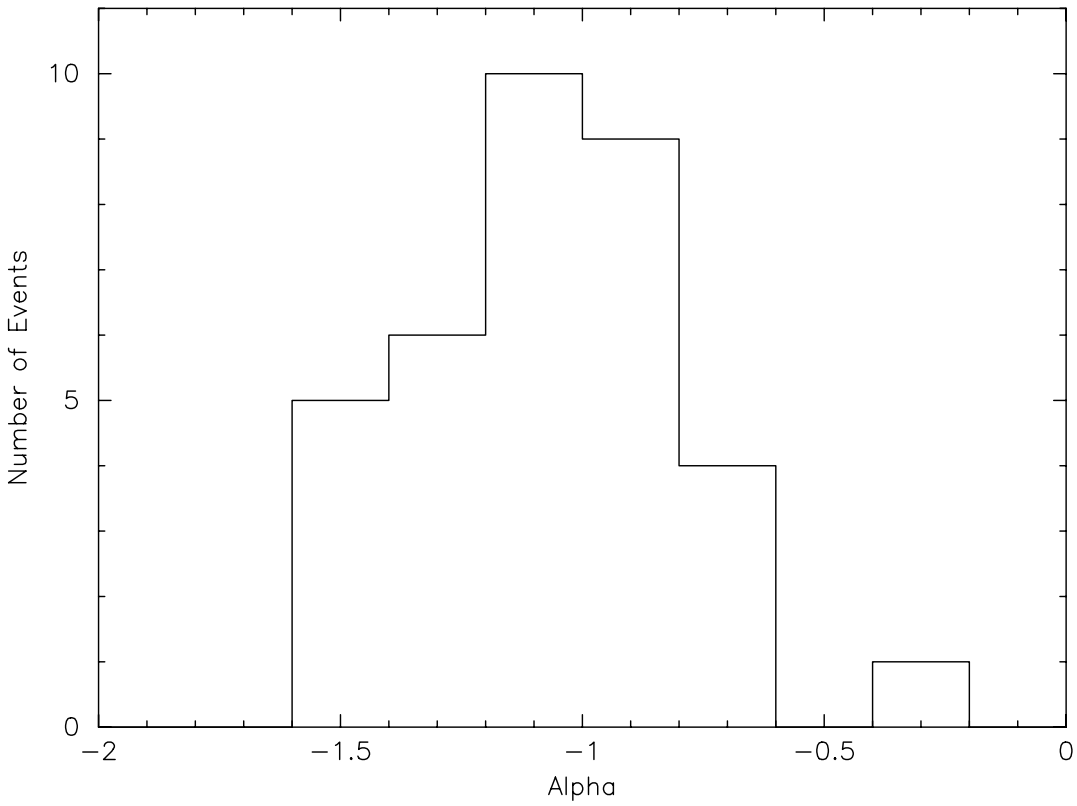

FIG. 6*b*

FIG. 6.—Distribution of the low-energy power-law index α for (*a*) each of the three kinds of bursts and (*b*) all of the bursts. (*a*) The hatched α-values are the burst spectra requiring the Band model, and the nonhatched α-values are the burst spectra that are adequately fit by the PLE model.

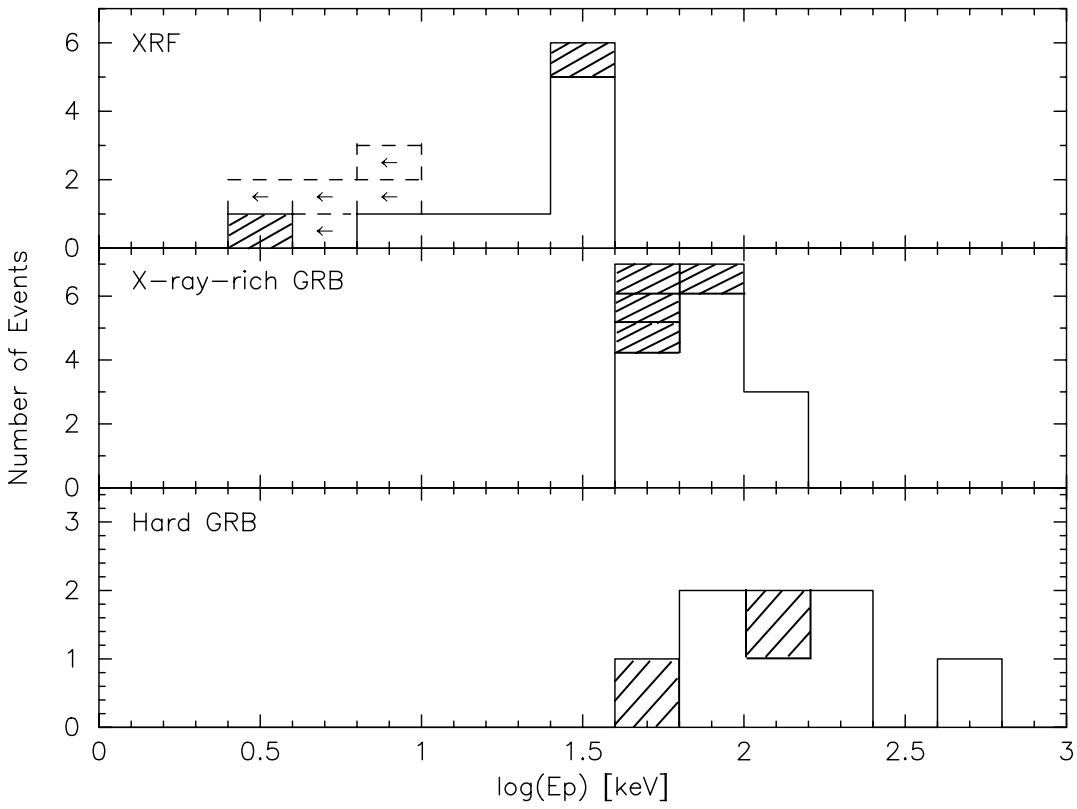

FIG. 7*a*

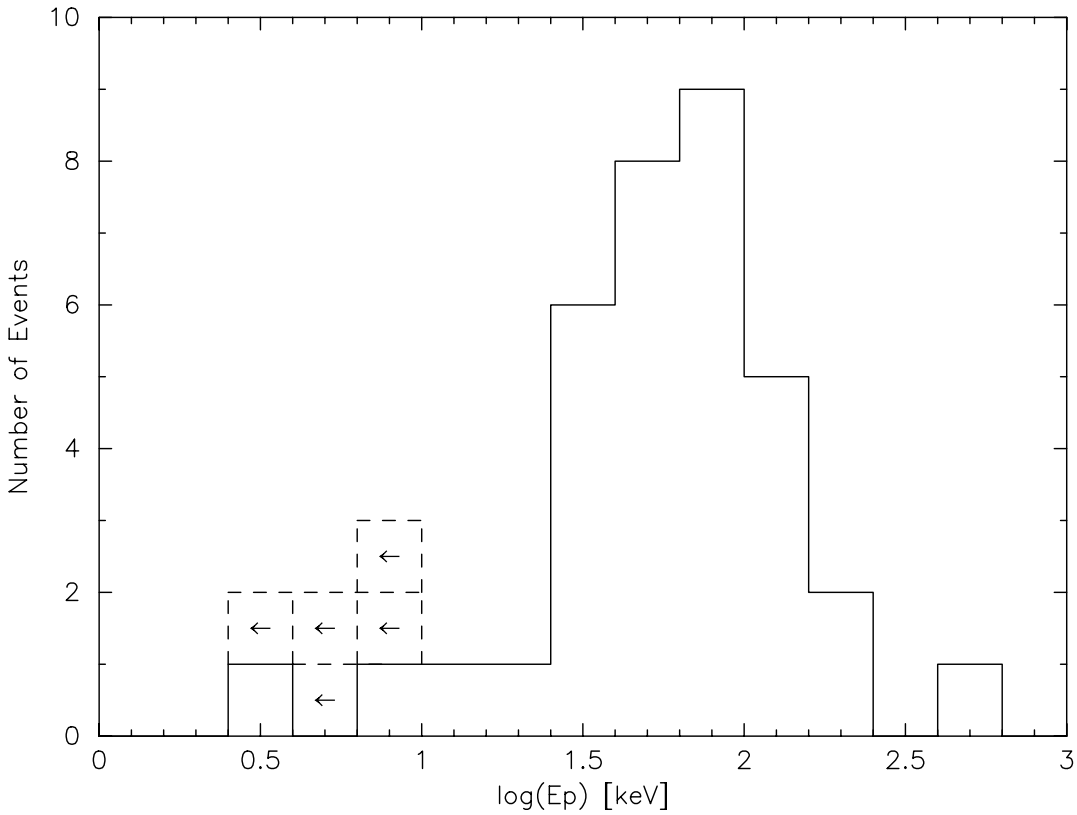

FIG. 7*b*

FIG. 7.—Distribution of E_{peak} for (*a*) each of the three kinds of bursts and (*b*) all of the bursts. (*a*) The hatched E_{peak} values are the burst spectra requiring the Band model, and the nonhatched E_{peak} values are the burst spectra that are adequately fit by the PLE model.

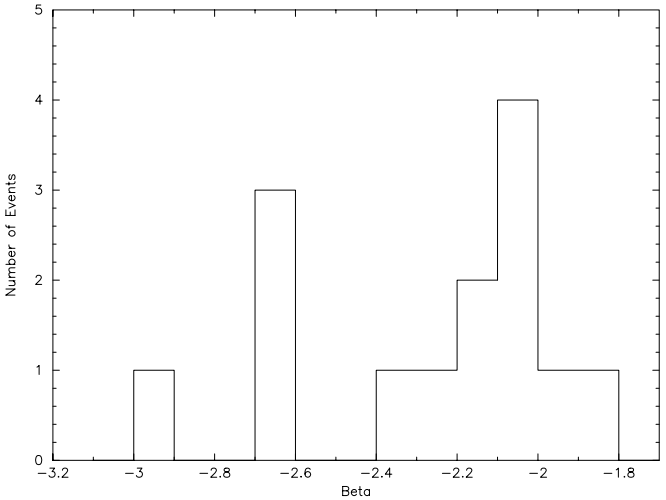

FIG. 8.—Distribution of the high-energy power-law index β for all of the bursts for which β could be determined. XRF 030723 is the burst with $\beta > -2$; in the case of this burst, we can say that $\beta > -2$ with high confidence, but the actual value of β is uncertain (Butler et al. 2005). We do not include two bursts (GRBs 020813 and 030519) with $\beta > -2$ in the sample, because the $E^{\rm obs}_{\rm peak}$ found by fitting to the *HETE-2* WXM and FREGATE data lies near or above the upper limit of the FREGATE energy band and is not the actual energy of the peak of the burst spectrum in νF_ν. Therefore the high-energy power law in the Band model that we fit to the *HETE-2* data is not the actual β in the Band-model spectrum.

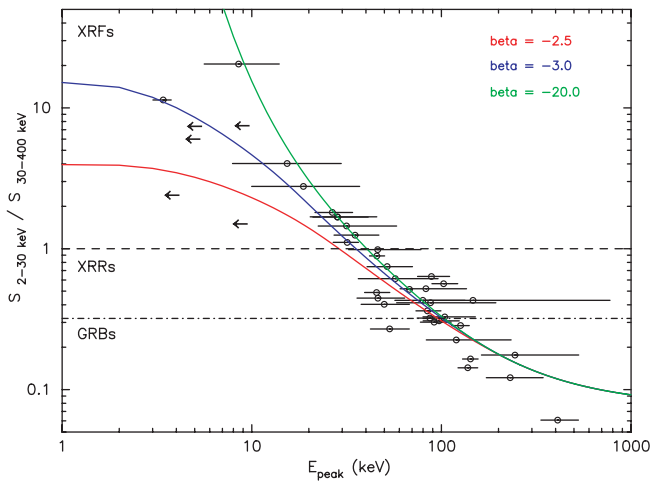

FIG. 9.—Distribution of bursts in the [$E_{\rm peak}$, $S_E(2-30\ {\rm keV})/S_E(30-400\ {\rm keV})$] plane. Overlaid are curves corresponding to the X-ray–to–γ-ray fluence ratio as a function of $E^{\rm obs}_{\rm peak}$, assuming the Band function with $\alpha = -1$, and $\beta = -2.5$ (*red*), -3.0 (*blue*), and -20.0 (*green*).

The distribution of β-values is shown in Figure 8. Because of the small number of GRBs with well-determined β-values, only the distribution for all of the GRB classes taken together is plotted. This distribution is similar to that for long BATSE bursts (Preece et al. 2000).

7. CORRELATIONS BETWEEN $E^{\rm obs}_{\rm peak}$ AND OTHER BURST PROPERTIES

Figure 9 shows the distribution of observed peak energy $E^{\rm obs}_{\rm peak}$ versus the fluence ratio $S_E(2-30\ {\rm keV})/S_E(30-400\ {\rm keV})$. Since the fluence ratio is independent of the normalization parameter of the model spectrum, it is possible to calculate the relationship between the fluence ratio and $E^{\rm obs}_{\rm peak}$. The overlaid curves in Figure 9 are the calculated relationships, assuming the Band function, for $\alpha = -1$ and $\beta = -2.5$ (*red*), -3.0 (*blue*), and -20.0 (*green*). The dependence of the fluence ratio on β is weak when $E^{\rm obs}_{\rm peak}$ is greater than 30 keV, and understandably becomes strong when $E^{\rm obs}_{\rm peak}$ is less than 30 keV. This implies that the choice of the proper spectral model is important for determining the fluence ratio, and for determining which bursts are XRFs and XRRs. Fortunately, the importance of choosing the correct spectral model for the latter is modest because a range in β of -2 to -20 produces a range in the fluence ratio of only 40% at $E^{\rm obs}_{\rm peak} = 30$ keV, which corresponds to the boundary between XRFs and XRRs.

Figure 10 shows the distribution of α-values (*left panel*) and β-values (*right panel*) versus $E^{\rm obs}_{\rm peak}$. The values of α and β show no statistically significant correlation with $E^{\rm obs}_{\rm peak}$ and therefore none with the kind of burst. Kippen et al. (2003) also found no statistically significant correlation between α and $E^{\rm obs}_{\rm peak}$ in the *BeppoSAX* WFC/*CGRO* BATSE sample of XRFs and GRBs.

Figure 11 shows the distribution of the bursts in this study in the [$S_E(2-400\ {\rm keV})$, $E^{\rm obs}_{\rm peak}$] plane. This figure shows that there is a strong correlation between $S_E(2-400\ {\rm keV})$ and $E^{\rm obs}_{\rm peak}$. The best-fit power-law slope between $E^{\rm obs}_{\rm peak}$ and $S_E(2-400\ {\rm keV})$ is 0.279 ± 0.053. The values of the slope and the uncertainty in it that we find imply a significance for the correlation of $\sim 15\ \sigma$. The correlation coefficient of +0.511 that we find between the two quantities also implies a high significance for the correlation. The probability of such a correlation occurring by chance for the sample size of 40 bursts is 3.0×10^{-4}. Thus, while the scatter in the correlation is large, the significance of the correlation is also large.

Figures 12 and 13 show the distribution of *HETE-2* bursts in the [$F^P_N(2-400\ {\rm keV})$, $E^{\rm obs}_{\rm peak}$] plane and the [$F^P_N(50-300\ {\rm keV})$, $E^{\rm obs}_{\rm peak}$] plane, respectively. There is no evidence for a correlation between $E^{\rm obs}_{\rm peak}$ and the peak photon flux $F^P_N(2-400\ {\rm keV})$, but a strong correlation exists between $E^{\rm obs}_{\rm peak}$ and the peak photon flux $F^P_N(50-300\ {\rm keV})$. The correlation coefficient of +0.802 that we find between the two quantities implies a high significance for the correlation. The probability of such a correlation occurring by chance for the sample size of 40 bursts is 3.9×10^{-7}. Thus, while the scatter in the correlation is large, the significance of the correlation is also large. Kippen et al. (2003) suggested a similar correlation for the *BeppoSAX* WFC/*CGRO* BATSE sample of XRFs and GRBs.

However, the correlation between $E^{\rm obs}_{\rm peak}$ and $F^P_N(50-300\ {\rm keV})$ is an artifact of the choice of 50–300 keV for the energy band in which the peak flux is measured. The reason is that for GRBs, $F^P_N(50-300\ {\rm keV})$ is roughly the *bolometric* peak photon number flux, whereas for XRRs, and especially for XRFs, $F^P_N(50-300\ {\rm keV})$ is clearly not the bolometric peak photon number flux. This is because $E^{\rm obs}_{\rm peak}$ lies near or below the lower limit of this energy band for XRRs, and far below the lower limit of the energy band for XRFs. The result is that the peak photon number fluxes for these bursts are greatly reduced from their bolometric values, as can be clearly seen by comparing Figures 12 and 13. The correlation coefficient for the distribution of bursts in the latter plane is only 0.297. Consequently, the significance of the correlation is only 94% for the sample size of 40 bursts.

Figures 14 and 15 compare the distributions of *HETE-2* bursts and *BeppoSAX* XRRs and GRBs, but not XRFs (Amati et al. 2002), in the [$S_E(2-400\ {\rm keV})$, $E^{\rm obs}_{\rm peak}$] plane and the [$F^P_N(2-400\ {\rm keV})$, $E^{\rm obs}_{\rm peak}$] plane, respectively. The distributions are similar, except that the XRFs are missing from the *BeppoSAX* distributions.

Figures 16 and 17 compare the distribution of *HETE-2* bursts in the [$F^P_N(50-300\ {\rm keV})$, $E^{\rm obs}_{\rm peak}$] plane with the distribution of

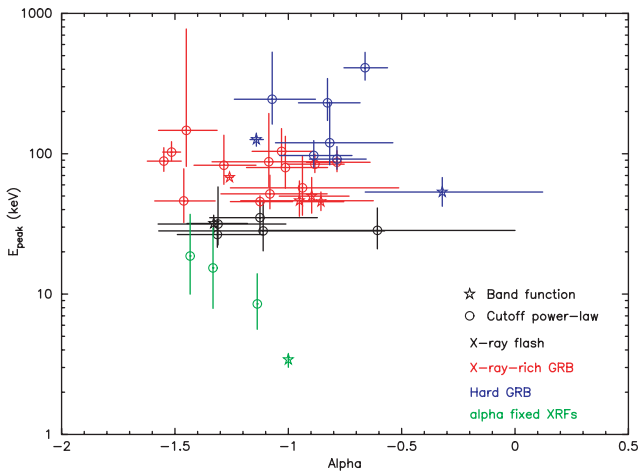

FIG. 10*a*

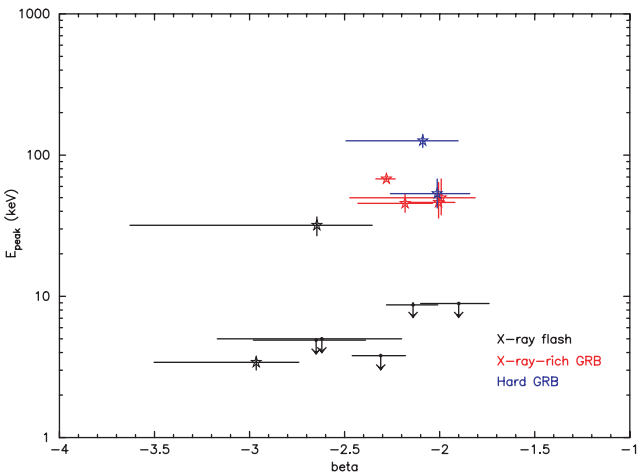

FIG. 10*b*

FIG. 10.—Low-energy power-law index (*a*) α and (*b*) β vs. $E^{\rm obs}_{\rm peak}$. The three kinds of bursts are denoted by different colors (XRF: *black*; XRR: *red*; and hard GRB: *blue*), and different symbols indicate the different best-fit spectral models (PLE model: *circles*; Band function: *stars*). Also plotted are the XRFs for which the value of α was fixed (*green*).

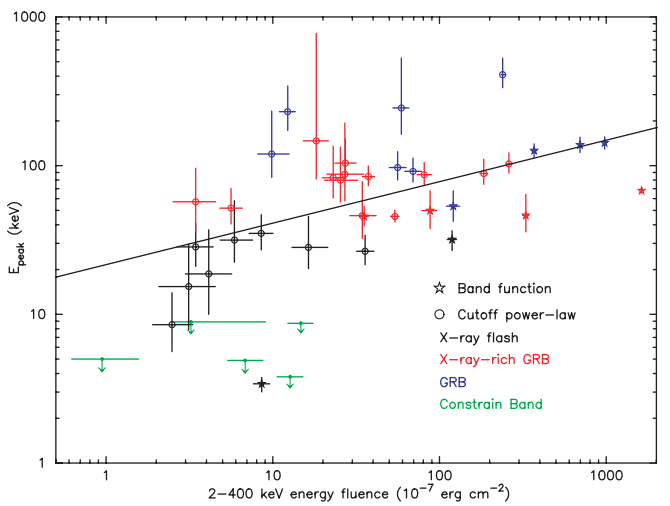

FIG. 11.—Distribution of bursts in the [S_E(2–400 keV), $E^{\rm obs}_{\rm peak}$] plane. The solid line is the best linear fit to the burst distribution, and is given by $E^{\rm obs}_{\rm peak} = (21.577 \pm 4.656) \times [S_E(2-400\ {\rm keV})/10^{-7}\ {\rm ergs\ cm^{-2}\ s^{-1}}]^{0.279\pm0.053}$. The correlation coefficient for the burst distribution is 0.511. The probability of such a correlation occurring by chance for the sample size of 40 bursts is 3.0×10^{-4}.

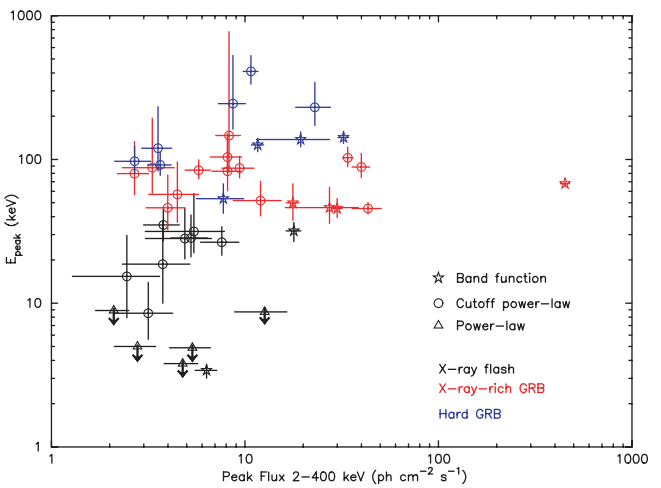

FIG. 12.—Distribution of bursts in the [F^P_N(2–400 keV), $E^{\rm obs}_{\rm peak}$] plane. The correlation coefficient for the burst distribution is 0.297. The significance of the correlation is only 94%.

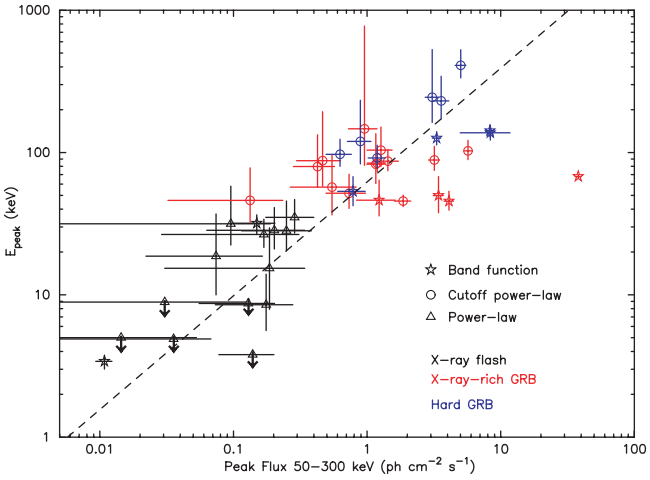

FIG. 13.—Distribution of bursts in the $[F_N^p(50\text{–}300\ \mathrm{keV}), E_{\mathrm{peak}}^{\mathrm{obs}}]$ plane. The dashed line corresponds to the best linear fit to the burst distribution, and is given by $E_{\mathrm{peak}}^{\mathrm{obs}} = (62.02 \pm 1.71) \times F_N^p(50\text{−}300\ \mathrm{keV})^{0.80\pm0.32}$. The correlation coefficient for the burst distribution is 0.802. The probability of such a correlation occurring by chance for the sample size of 40 bursts is 3.9×10^{-7}.

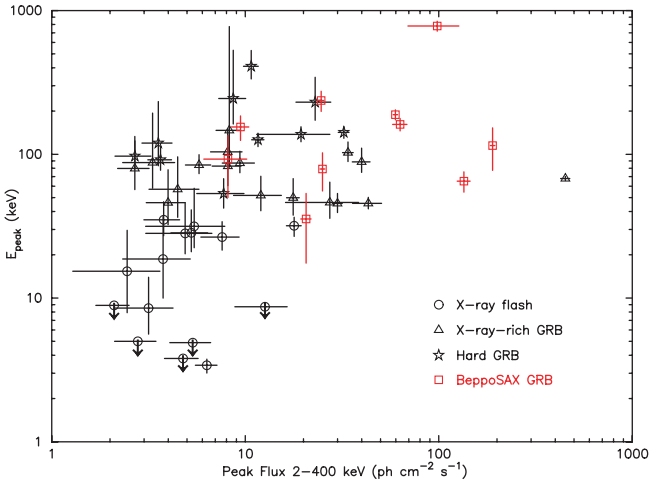

FIG. 15.—Comparison of the distributions of *HETE-2* bursts and *BeppoSAX* XRRs and GRBs, but not XRFs (Amati et al. 2002), in the $[F_N^p(2\text{–}400\ \mathrm{keV}), E_{\mathrm{peak}}^{\mathrm{obs}}]$ plane. The distributions are similar, except that the XRFs are missing from the *BeppoSAX* distribution.

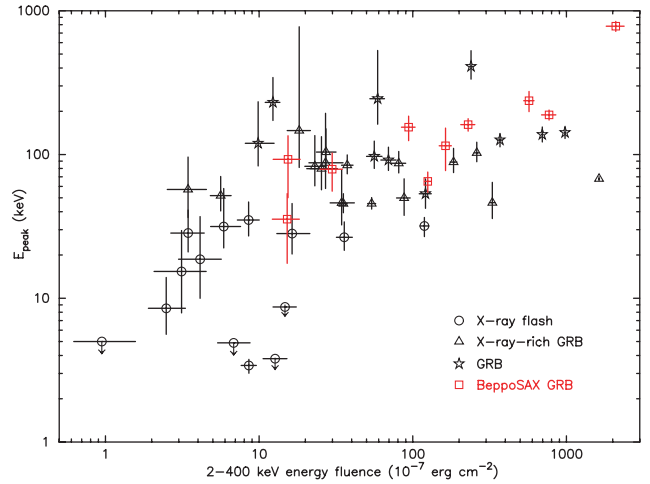

FIG. 14.—Comparison of the distributions of *HETE-2* bursts and *BeppoSAX* XRRs and GRBs, but not XRFs (Amati et al. 2002), in the $[S_E(2\text{–}400\ \mathrm{keV}), E_{\mathrm{peak}}^{\mathrm{obs}}]$ plane. The distributions are similar, except that the XRFs are missing from the *BeppoSAX* distribution.

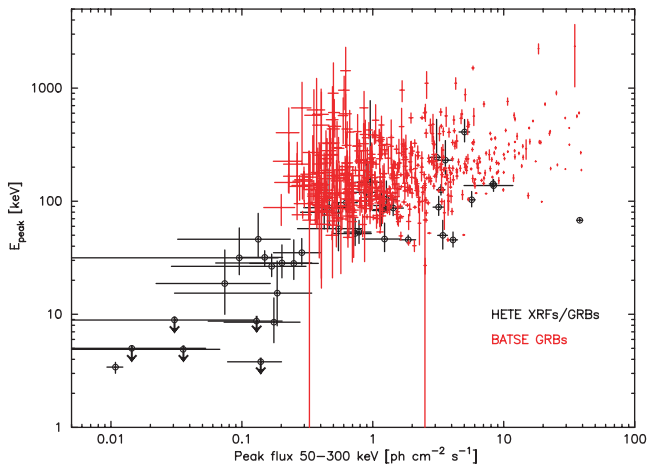

FIG. 16.—Distribution of *HETE-2* bursts (*black*) and BATSE bursts (*red*) in the $[F_N^p(50\text{–}300\ \mathrm{keV}), E_{\mathrm{peak}}^{\mathrm{obs}}]$ plane.

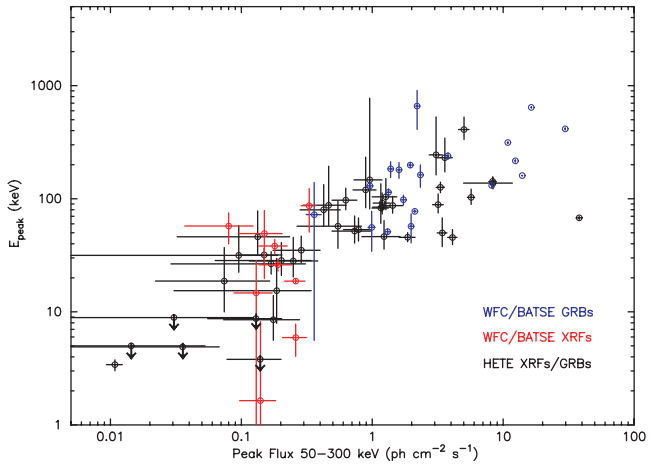

FIG. 17.—Distribution of *HETE-2* bursts (*black*) and WFC BATSE bursts (*red* and *blue*) in the [F_N^P(50–300 keV), E^{obs}_{peak}] plane.

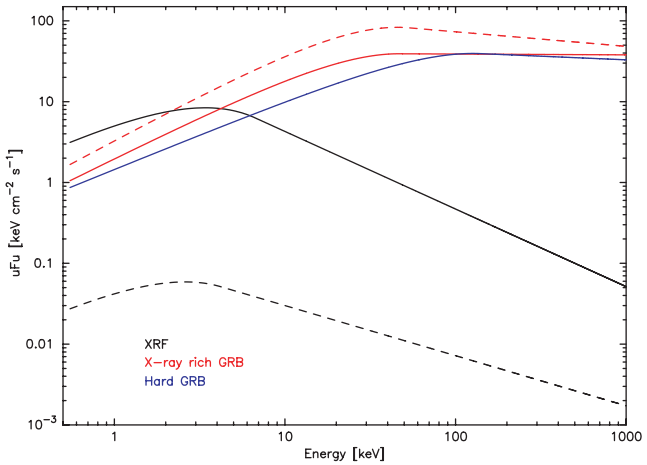

FIG. 18.—Examples of best-fit νF_ν spectra for XRFs GRB 010213 (*black solid line*) and GRB 020903 (*black dashed line*), XRRs GRB 010613 (*red solid line*) and GRB 021211 (*red dashed line*), and hard GRB 030328 (*blue solid line*).

long BATSE bursts (Band et al. 2004) and the distribution of WFC BATSE bursts and a representative sample of long BATSE GRBs (Kippen et al. 2003), respectively, in the same plane. The distribution of *HETE-2* bursts is consistent with the distribution of BATSE bursts for $E^{obs}_{peak} > 50$ keV but extends farther down in E^{obs}_{peak} [and therefore in F_N^P(50–300 keV)]. This is expected because of the BATSE trigger threshold, which is 50 keV. The distribution of *HETE-2* bursts is consistent with the distribution of WFC BATSE bursts but also extends down to fainter peak photon number fluxes for a similar reason.

8. DISCUSSION

8.1. *Comparison of XRF, XRR, and GRB Properties*

We have studied the global properties of 45 GRBs localized by the *HETE-2* WXM during the first 3 years of its mission, focusing on the properties of XRFs and XRRs. We find that the numbers of XRFs, XRRs, and GRBs are comparable for bursts localized by the *HETE-2* WXM. We find that there is no statistically significant evidence for any difference in the duration distributions or the sky distributions of the three kinds of bursts. We also find that the spectral properties of XRFs and XRRs are similar to those of GRBs, except that the values of the peak energy E^{obs}_{peak} of the burst spectrum in νF_ν, the peak flux F_{peak}, and the fluence S_E of XRFs are much smaller—and those of XRRs are smaller—than those of GRBs. Figure 18, which shows the best-fit νF_ν spectra of two XRFs, two XRRs, and two GRBs, illustrates this. Our results are consistent with Barraud et al. (2003), who studied the spectral properties of the *HETE-2* GRBs using FREGATE data. Finally, we find that the distributions of all three kinds of bursts form a continuum in the [S(2–30 keV), S(30–400 keV)] plane, the [S(2–400 keV), E_{peak}] plane, and the [F_{peak}(50–300 keV), E^{obs}_{peak}] plane. These results provide strong evidence that all three kinds of bursts arise from the same phenomenon.

8.2. *Theoretical Models of XRFs*

Several theoretical models of XRFs have been proposed. GRBs at very high redshifts might be observed as XRFs (Heise et al. 2001). However, the fact that the duration distribution for XRFs is similar to that for GRBs argues against this hypothesis as the explanation for most XRFs, as do the low redshifts (Soderberg et al. 2004; Fynbo et al. 2004) and the redshift constraints (Bloom et al. 2003) that exist for several XRFs.

According to Mészáros et al. (2002) and Woosley et al. (2003), X-ray (20–100 keV) photons are produced effectively by the hot cocoon surrounding the GRB jet as it breaks out, and could produce XRF-like events if viewed well off the axis of the jet. However, it is not clear that such a model would produce roughly equal numbers of XRFs, XRRs, and GRBs, or the nonthermal spectra exhibited by XRFs.

Yamazaki et al. (2002, 2003) have proposed that XRFs are the result of a highly collimated GRB jet viewed well off the axis of the jet. In this model, the low values of E_{peak} and E_{iso} (and therefore of E^{obs}_{peak} and S_E) seen in XRFs are the result of relativistic beaming. However, it is not clear that such a model can produce roughly equal numbers of XRFs, XRRs, and GRBs, and still satisfy the observed relation between E_{iso} and E_{peak} (Amati et al. 2002; D. Q. Lamb et al. 2005b, in preparation).

The "dirty fireball" model of XRFs posits that baryonic material is entrained in the GRB jet, resulting in a bulk Lorentz factor $\Gamma \ll 300$ (Dermer et al. 1999; Huang et al. 2002; Dermer and Mitman 2003). At the opposite extreme, GRB jets in which the bulk Lorentz factor $\Gamma \gg 300$ and the contrast between the bulk Lorentz factors of the colliding relativistic shells in the internal shock model are small can also produce XRF-like events (Mochkovitch et al. 2003).

It has been proposed that XRFs are due to universal GRB jets in which the luminosity falls off like a power law from the jet axis (Zhang & Mészáros 2002; Rossi et al. 2002) and are viewed well off the jet axis (Zhang et al. 2004). However, Lamb et al. (2005) have shown that such a model predicts far more XRFs than GRBs, in conflict with the *HETE-2* results described in this paper. A universal GRB jet model in which the luminosity falls off like a Gaussian may do better (Zhang et al. 2004).

Lamb et al. (2005) have shown that a unified description of XRFs, XRRs, and GRBs is possible in a model in which the GRB jet opening angle varies over a wide range. In this model, XRFs are due to jets with wide opening angles, while GRBs are due to jets with narrow opening angles.

As this discussion suggests, understanding the properties of XRFs and XRRs, and clarifying the relationship between these two kinds of events and GRBs, could provide a deeper understanding of the prompt emission of GRBs. And as Lamb et al.

(2005) have emphasized, XRFs may provide unique insights into the nature of GRB jets, the rate of GRBs, and the relationship between GRBs and Type Ic supernovae.

9. CONCLUSIONS

We have studied the global properties of 45 GRBs observed by *HETE-2* during the first 3 years of its mission, focusing on the properties of XRFs and XRRs. We find that the numbers of XRFs, XRRs, and GRBs are comparable. We find that the durations and the sky distributions of XRFs and XRRs are similar to those of GRBs. We also find that the spectral properties of XRFs and XRRs are similar to those of GRBs, except that the values of the peak energy $E_{\rm peak}^{\rm obs}$ of the burst spectrum in νF_ν, the peak flux $F_{\rm peak}$, and the fluence S_E of XRFs are much smaller—and those of XRRs are smaller—than those of GRBs. Finally, we find that the distributions of all three kinds of bursts form a continuum in the [S(2–30 keV), S(30–400 keV)] plane, the [S(2–400 keV), $E_{\rm peak}$] plane, and the [$F_{\rm peak}$(50–300 keV), $E_{\rm peak}^{\rm obs}$] plane. These results provide strong evidence that all three kinds of bursts arise from the same phenomenon. They also provide constraints on theoretical models of XRFs.

We would like to thank R. Marc Kippen for providing the WFC BATSE spectral parameters. We would also like to thank the anonymous referee for comments and suggestions that materially improved the paper. The *HETE* mission is supported in the US by NASA contract NASW-4690; in Japan, in part by the Ministry of Education, Culture, Sports, Science, and Technology grant-in-aid 12440063; and in France by CNES contract 793-01-8479. K. Hurley is grateful for *HETE* support under contract MIT-SC-R-293291.

REFERENCES

Amati, L., et al. 2002, A&A, 390, 81
Atteia, J-L, et al. 2003, in AIP Conf. Proc. 662, Gamma-Ray Burst and Afterglow Astronomy, ed. G. R. Ricker & R. Vanderspek (New York: AIP), 17
Band, D. L., Norris, J. P., & Bonnell, J. T. 2004, ApJ, 613, 484
Band, D. L., et al. 1993, ApJ, 413, 281
Barraud, C., et al. 2003, A&A, 400, 1021
Bloom, J. S., et al. 2003, ApJ, 599, 957
Butler, N. R., et al. 2005, ApJ, 621, 884
Dermer, C. D., Chiang, J., & Böttcher, M. 1999, ApJ, 513, 656
Dermer, C. D., & Mitman, K. E. 2003, in ASP Conf. Ser. 312, Third Rome Workshop on Gamma-Ray Bursts in the Afterglow Era, ed. M. Feroci et al. (San Francisco: ASP), 301
Fenimore, E. E., in't Zand, J. J. M., Norris, J. P., Bonnel, J. T., & Nemiroff, R. J. 1995, ApJ, 448, L101
Fynbo, J. P. U., et al. 2004, ApJ, 609, 962
Heise, J., in't Zand, J., Kippen, R. M., & Woods, P. M. 2001, in Gamma-Ray Bursts in the Afterglow Era, ed. E. Costa, F. Frontera, & J. Hjorth (Berlin: Springer), 16
Huang, Y. F., Dai, Z. G., & Lu, T. 2002, MNRAS, 332, 735
Kawai, N., et al. 2003, in AIP Conf. Proc. 662, Gamma-Ray Bursts and Afterglow Astronomy 2001, ed. G. R. Ricker & R. Vanderspek (New York: AIP), 25
Kippen, R. M., Woods, P. M., Heise, J., in't Zand, J., Briggs, M. S., & Preece, R. D. 2003, in AIP Conf. Proc. 662, Gamma-Ray Bursts and Afterglow Astronomy 2001, ed. G. R. Ricker & R. Vanderspek (New York: AIP), 244
Lamb, D. Q., Donaghy, T. Q., & Graziani, C. 2005, ApJ, 620, 355
Mallozzi, R. S., Paciesas, W. S., Pendleton, G. N., Briggs, M. S., Preece, R. D., Meegan, C. A., & Fishman, G. J. 1995, ApJ, 454, 597
Mészáros, P., Ramirez-Ruiz, E., Rees, M. J., & Zhang, B. 2002, ApJ, 578, 812
Mochkovitch, R., Daigne, F., Barraud, C., & Atteia, J. L. 2003, in ASP Conf. Ser. 312, Third Rome Workshop on Gamma-Ray Bursts in the Afterglow Era, ed. M. Feroci et al. (San Francisco: ASP), 381
Norris, J. P., Marani, G. F., & Bonnell, J. T. 2000, ApJ, 534, 248
Olive, J.-F., et al. 2003, in AIP Conf. Proc. 662, Gamma-Ray Bursts and Afterglow Astronomy 2001, ed. G. R. Ricker & R. Vanderspek (New York: AIP), 88
Paciesas, W. S., et al. 1999, ApJS, 122, 465
Preece, R. D., Briggs, M. S., Mallozzi, R. S., Pendleton, G. N., & Paciesas, W. S. 2000, ApJS, 126, 19
Rossi, E., Lazzati, D., & Rees, M. J. 2002, MNRAS, 332, 945
Sakamoto, T., et al. 2004, ApJ, 602, 875
Shirasaki, Y., et al. 2003, PASJ, 55, 1033
Soderberg, A. M., et al. 2004, ApJ, 606, 994
Woosley, S. E., Zhang, W., & Heger, A. 2003, in AIP Conf. Proc. 662, Gamma-Ray Bursts and Afterglow Astronomy 2001, ed. G. R. Ricker & R. Vanderspek (New York: AIP), 185
Yamazaki, R., Ioka, K., & Nakamura, T. 2002, ApJ, 571, L31
———. 2003, ApJ, 593, 941
Zhang, B., Dai, X., Lloyd-Ronning, N. M., & Mészáros, P. 2004, ApJ, 601, L119
Zhang, B., & Mészáros, P. 2002, ApJ, 571, 876